Impact Crater Formation in Icy Layered Terrains on Mars

Citation	Senft, Laurel E., and Sarah T. Stewart. 2008. Impact crater formation in icy layered terrains on Mars. Meteoritics and Planetary Science 43: 1993–2013.
Published Version	http://meteoritics.org/
Accessed	February 18, 2015 12:08:30 AM EST
Citable Link	http://nrs.harvard.edu/urn-3:HUL.InstRepos:4727388
Terms of Use	This article was downloaded from Harvard University's DASH repository, and is made available under the terms and conditions applicable to Other Posted Material, as set forth at http://nrs.harvard.edu/urn-3:HUL.InstRepos:dash.current.terms-of-use#LAA

(Article begins on next page)

Impact crater formation in icy layered terrains on Mars

Laurel E. SENFT[*] and Sarah T. STEWART

Department of Earth and Planetary Sciences, Harvard University, 20 Oxford Street, Cambridge, Massachusetts 02138, USA
[*]Corresponding author. E-mail: lsenft@fas.harvard.edu

Abstract–We present numerical simulations of crater formation under Martian conditions with a single near-surface icy layer to investigate changes in crater morphology between glacial and interglacial periods. The ice fraction, thickness, and depth to the icy layer are varied to understand the systematic effects on observable crater features. To accurately model impact cratering into ice, a new equation of state table and strength model parameters for H_2O are fitted to laboratory data. The presence of an icy layer significantly modifies the cratering mechanics. Observable features demonstrated by the modeling include variations in crater morphometry (depth and rim height) and icy infill of the crater floor during the late stages of crater formation. In addition, an icy layer modifies the velocities, angles, and volumes of ejecta, leading to deviations of ejecta blanket thickness from the predicted power law. The dramatic changes in crater excavation are a result of both the shock impedance and the strength mismatch between layers of icy and rocky materials. Our simulations suggest that many of the unusual features of Martian craters may be explained by the presence of icy layers, including shallow craters with well-preserved ejecta blankets, icy flow related features, some layered ejecta structures, and crater lakes. Therefore, the cratering record implies that near-surface icy layers are widespread on Mars.

INTRODUCTION

Icy and layered surfaces are seen throughout the solar system. For example, low strength sedimentary layers are abundant on the Earth and Mars (Malin and Edgett 2000; Edgett and Malin 2002; Beyer and McEwen 2005), and a low strength regolith layer covers the moon (Gault et al. 1966). The icy satellites are composed of large scale layers of ice and rock with varying ice phases and volatile contents (Schenk 2002; Showman and Malhotra 1999), and even comets may be layered rubble piles (Belton et al. 2007). Despite their common occurrence, layers are difficult to study because they are often buried and hidden from view. However, because crater morphologies are dependent on subsurface material properties, impact craters provide a powerful means to probe the properties of near-surface layers. Furthermore, cratering is an ubiquitous process in our solar system; thus, surfaces of all ages and locations on a planet can be studied using the same methods. Thus, several cratering studies have focused on understanding the role of layers in the cratering process.

Laboratory and numerical experiments have shown significant changes in crater and ejecta blanket morphologies with strength contrasts in the target. Strength layers modify ejection angles, and a target with weaker layers will undergo more collapse, resulting in shallower craters with terraces and benches (Oberbeck and Quaide 1967; Quaide and Oberbeck 1968; Piekutowski 1977; Schultz 1992; Head et al. 2002; Senft and Stewart 2007). Numerical studies of impacts into marine (layered water over rock) targets have displayed morphologic variations that are dependent upon the thickness of the water layer and the size of the impactor (Ormö et al. 2002; Shuvalov and Trubestkaya 2002; Ormö et al. 2004). Marine impact simulations have been used to explain the morphology of the Lockne impact structure in Sweden (Lindstrom et al. 2005), the Chesapeake Bay impact structure in Virginia (Collins and Wünnemann 2005), and the Mjølnir impact structure in the Barents Sea (Shuvalov et al. 2002).

A problem which has not been extensively studied is the effect of icy layers. Icy layers pose additional challenges compared to strength variations in rocky surfaces because there is a substantial equation of state difference as well as a large strength difference. Numerical studies of marine impacts did not have to grapple with the complex strength of ice, and only needed to consider water at the surface (whereas ice can be buried in complex geometries). Understanding the observable features from cratering in icy, layered surfaces may lead to inferences about subsurface structures on many bodies in the solar system. In particular, icy layers provide

clues to the climatic history on Mars. Mars is believed to have undergone significant variations in global climate, including the possibility of a warmer, wetter early period (e.g., Fanale et al. 1992; Owen 1992; Phillips et al. 2001; Poulet et al. 2005 Bibring et al. 2006) and recent rapid climate excursions resulting from obliquity changes (e.g., Laskar et al. 2004).

Widespread near-surface ice deposits are inferred on Mars. Results from the neutron spectrometer on Mars Odyssey imply that near surface (upper meter) ground ice is abundant poleward of 40 degrees latitude (Boynton et al. 2002; Feldman et al. 2002; Mitrofanov et al. 2002), in agreement with theoretical studies of ground ice stability under current climatic conditions (Clifford and Hillel 1983; Clifford 1993; Mellon and Jakosky 1995). However, the neutron spectrometer data also discovered hydrogen enrichment (which can be interpreted as subsurface ice or ice and hydrogen-rich minerals) at lower latitudes. The Martian obliquity varies drastically over time (with time scales of 10^4–10^5 years), with a time-averaged value of about 38 degrees and a maximum value of about 82 degrees (current value is about 25 degrees). Obliquity variations dramatically affect the ground ice stability pattern; for example, at 32 degrees or greater obliquity, near surface ground ice is stable globally (Laskar et al. 2004). Climate modeling shows that during periods of high obliquity, ice from the poles may be transported and deposited at mid- to tropical-latitudes (Jakosky and Carr 1985; Mischna et al. 2003; Levrard et al. 2004; Forget et al. 2006), leading to the deposition of ice rich layers on the surface. To explain the observed km-scale thickness of viscous layers of material, Milliken et al. (2003) suggest that a portion of a glacial deposit (protected by a lag deposit) may remain stable between glacial cycles, building up thicker ice-rich layers over time. A dissected (formerly ice-rich) mantling deposit located between 30–60 degrees north and south latitudes, associated viscous flow features and gullies, and mid-latitude glaciers are interpreted to be remnants from the last high obliquity period ("ice age") that occurred from approximately 2.1 to 0.4 Myr (Mustard et al. 2001; Head et al. 2003; Neukum et al. 2004; Head et al. 2005; Head et al. 2006). It is also possible that deeper deposits of ground ice could be built up and preserved by groundwater flow (Clifford 1993). Finally, icy layers may be a contributing factor to the layered ejecta structures found around the majority of Martian impact craters (e.g., Carr et al. 1977; Gault and Greeley 1978; Mouginis-Mark 1981; Barlow and Perez 2003; Komatsu et al. 2007; Black and Stewart 2008).

In this work, we use numerical simulations to explore and quantify the effects of icy surface and subsurface layers on crater formation, with a focus on understanding Martian crater forms. We conduct simulations of impacts onto targets with a single icy layer within an otherwise uniform basalt crust. We vary the burial depth, thickness, and ice fraction of this layer as well as the size of the impactor (sections Method and Results). The target geometries in these simulations are a simplification of the Martian upper crust, and are not intended to exactly reproduce specific Martian craters, but to investigate and illustrate the range of possible observable features resulting from the presence of near-surface icy layers. The results are compared to observations of Martian impact craters, and we show that some of the anomalous features of these craters (compared to craters on non-icy terrestrial planets) may be explained by the presence of icy layers in the target (Discussion section).

METHOD

Cratering simulations are conducted using CTH, an Eulerian shock physics code developed at Sandia National Laboratories (McGlaun et al. 1990). CTH includes an adaptive mesh refinement (AMR) feature, meaning smaller-scale features (such as fine layers near the surface, the ejecta curtain, and the shock wave) can be resolved without expending too much computational energy elsewhere in the problem domain (Crawford 1999). AMR refines and unrefines the mesh according to user defined indicators; for example, indicators are chosen to refine free surfaces and the leading edge of shock waves. All of the simulations presented in this paper use two dimensional cylindrical symmetry. The validity of a numerical cratering calculation is strongly dependent upon the strength model and equation of state chosen for the materials involved in the problem; thus, particular care was applied to these areas.

Strength Model

The strength model describes the response of a material to deviatoric stresses; for this work, we develop new strength parameters for H_2O based on laboratory data. We use the strength model developed by Collins et al. (2004) and implemented into CTH by Senft and Stewart (2007). In this model, shear strength is linearly degraded from an intact strength value (strength controlled by the creation of new fractures) to a fragmented (strength controlled by friction) value. A dimensionless scalar variable called damage is introduced to track this degradation; completely intact rock has a damage of zero, and completely fragmented rock has a damage of one. Thus, shear strength is a function of damage, temperature, and pressure, and tensile strength is a function of damage. Bulking (decrease in density due to fracturing) is not included in the calculations. Sediments or regolith can be approximated by initializing a calculation with an initial damage of one. Strength parameters are chosen by fitting quasi-static laboratory test data. For basalt, we use the yield surface presented in Pierazzo et al. (2005), and dynamic tensile strength data from Cohn and Ahrens (1981). For ice, we use uniaxial compressive strength temperature dependence data from Arakawa and Maeno (1997), friction data from Beeman et al. (1988), dynamic tensile strength data from Lange and
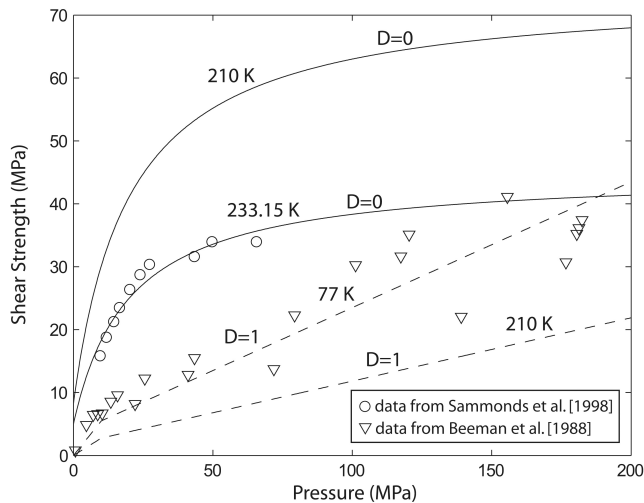
Fig. 1. Example yield surfaces in the ice strength model at different temperatures and damage levels. Shear strength is defined in terms of the square root of the second invariant of the deviatoric stress tensor, $\sqrt{J_2}$, for fragmented (damaged) ice (i.e., ice-on-ice friction; dashed lines) and intact ice (solid lines). Circles are data at 233.15 K from Sammonds et al. (1998), and triangles are data at 77 K from Beeman et al. (1988). The strength curves at 210 K, a mean Martian surface temperature, are used in this work.

Ahrens (1983), and triaxial shear strength data from Sammonds et al. (1998). Figure 1 shows the shear strength data of intact (non-damaged) ice from Sammonds et al. (1998) (circles) and the shear strength data of fragmented (damaged) ice from Beeman et al. (1988) (triangles). Note that the data was not collected at the same temperatures used in the simulations, and that the strength of ice has strong temperature dependence. We fit a temperature degradation function to uniaxial compression data from Arakawa and Maeno (1997) and use this to calculate the yield surface at other temperatures. The intact and damaged shear strength curves at 210 K, the Martian surface temperature assumed in the calculations presented in this paper, are shown in Fig. 1. The method outlined above assumes that the temperature dependence for uniaxial compressive strength is the same as the temperature dependence at higher pressures and that intact and fragmented ice have the same temperature dependences. In reality, this will not be true; for instance, the coefficient of friction of ice is not significantly temperature dependent until very close to the melting point, and also depends upon a number of other factors which have been neglected (such as strain rate). However, these effects are small compared to the larger effect of the strength contrast between ice and basalt. We choose tensile strengths that are somewhat lower than those measured in quasi-state laboratory tests to account for the strong scale dependence on tensile strength (Griffith 1920; Housen and Holsapple 1990, 1999).

Two modifications were made to the rock strength model since its initial implementation into CTH. First, temperature dependent tensile strength was removed, because tensile strength (particularly of ice) is less temperature dependent

than shear strength and the tensile strength of water and magma are comparable to the tensile strength of the solid (e.g., Croft et al. 1979; Zhang 1999; Boteler and Sutherland 2004). Second, the damaged shear strength function was modified to allow for a change in the coefficient of friction at higher pressures (e.g., Byerlee 1978).

The strength-damage model described above will not reproduce the morphology of craters above the simple to complex transition, for which an additional weakening mechanism is needed. Here we use acoustic fluidization (Melosh and Ivanov 1999) to aid complex crater collapse, and in the absence of better information, we assume that all materials have the same acoustic fluidization parameters. This assumption is supported by work by Bray et al. (2008, submitted), who show that similar acoustic fluidization parameters for ice and rock reproduce the morphology of central peak craters on the moon and Ganymede. We choose parameters that give a reasonable agreement to measured Martian crater geometries (Stewart and Valiant 2006) and that are in between the values used by Collins (2002) and Wünnemann and Ivanov (2003) for the moon.

The parameters of the strength model are listed in Table 1. For a complete description of the model parameters, see Senft and Stewart (2007). A complication not resolved here is the strength of ice-rock mixtures. When a cell with a mixture of materials is encountered in CTH, the shear stress of each material in the cell is separately calculated based on the yield surface for that material. Then, the average shear stress in the cell is calculated by volume averaging the component stresses. The average stress state is used to deform the material in the cell, and is advected in the Eulerian remap step. In reality, the rheologic properties of ice/rock mixtures are more complicated than simple volume averaging, and in fact, the weaker component may dominate the strength (e.g., Hiraoka et al. 2006). Hence, the current volume-averaging scheme provides a conservative limit for the observable effects from ice-rock mixtures.

Equation of State

The equation of state (EOS) describes the response of a material to volumetric stresses. We use Sesame-style tabular equations of state (Holian 1984), where pressure, energy, and entropy are tabulated over a density and temperature grid to allow for fast look-up and interpolation of the EOS. The basalt Sesame table (ρ_0 = 2820 kg/m³) was developed by Kerley (1999); the table is a density scaled version of the EOS for α-quartz and includes two solid phases (α-quartz and stishovite), a liquid phase with dissociation, and vapor. In a few cases, we considered surface sand deposits and used the Sesame table for dry sand (ρ_0 = 1600 kg/m³), which is based on fused quartz with the P-α pore compaction model (Herrmann 1969; Hertel and Kerley 1998).

We construct a new Sesame table for H_2O because pre-

Table 1. Strength parameters used to model basalt and ice. r_p is the radius of the projectile. For a complete description of the strength model, refer to Senft and Stewart (2007). In some simulations D_{sc} and D_{tc} are set to 1.0 (see text).

| Strength model parameters			
Variable	Description	Basalt	Ice
Y_o	Shear strength of intact rock at zero pressure and low temperatures	10 MPa	16.4 MPa
Y_m	Limiting shear strength as pressure increases at low temperatures	3.5 GPa	147 MPa
Y_c	Cohesion at zero pressure and low temperature	0 MPa	0 MPa
$_i$	Coefficient of internal friction of intact rock	1.2	6.54
$_{d,i}$	Coefficient of friction of fragmented rock (low pressure)	0.85	0.55
$_{d,h}$	Coefficient of friction of fragmented rock (high pressure)	0.6	0.2
$P_{tr,c}$	Transition pressure between $_{d,i}$ and $_{d,h}$	200 MPa	10 MPa
T_m	Melting temperature	1200 K	273.15 K
ξ	Thermal softening parameter	1.2	1.84
Y_{to}	Maximum tensile strength	−1 MPa	−0.17 MPa
P_{bd}	Brittle to ductile transition pressure	2.77 GPa	689 MPa
P_{bp}	Brittle to plastic transition pressure	4.11 GPa	699 MPa
K_o	Bulk modulus at ambient pressure and temperature	45 GPa	8.9 GPa
G	Shear modulus at ambient pressure and temperature	30 GPa	3.52 GPa
D_{so}	Initial shear damage	0.0	0.0
D_{to}	Initial tensile damage	0.0	0.0
η	Acoustic fluidization viscosity	No af for r_p 100 m 2.e8 Pa*s for r_p 800 m	No af for r_p 100 m 2.e8 Pa*s for r_p 800 m
τ	Acoustic fluidization decay constant	No af for r_p 100 m 32 s for r_p 800 m	No af for r_p 100 m 32 s for r_p 800 m
C_{vib}	Maximum vibration particle velocity (fraction of the maximum velocity)	No af for 100 m 0.25 for r_p 800 m	No af for r_p 100 m 0.25 for r_p 800 m
t_{off}	Time to turn off new acoustic fluidization pressure vibrations	No af for r_p 100 m 60 s for r_p 800 m	No af for r_p 100 m 60 s for r_p 800 m
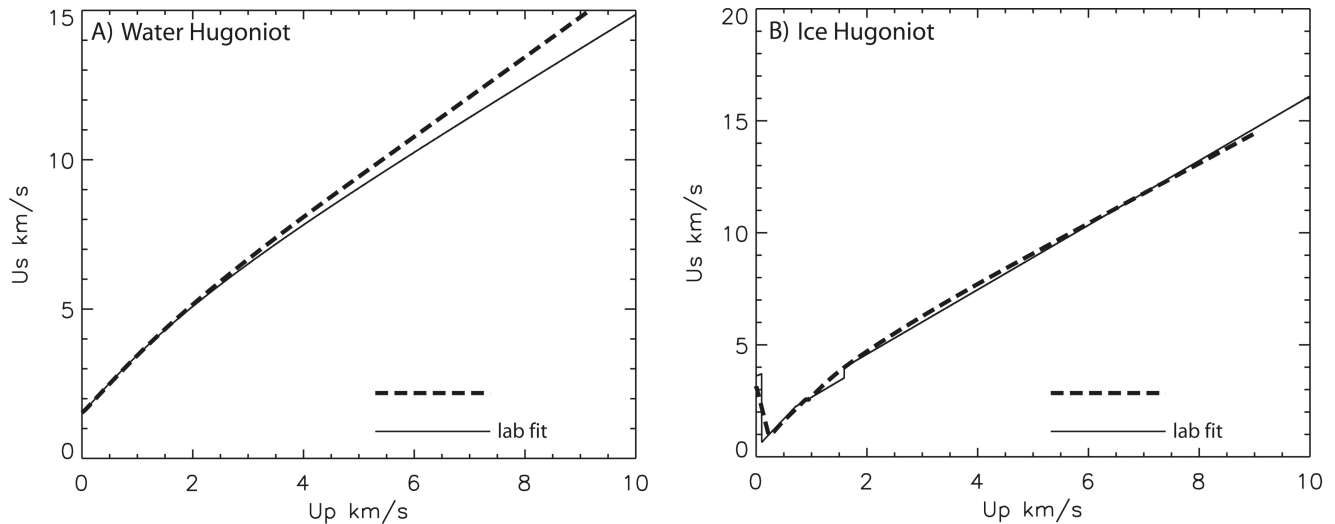
Fig. 2. Shock Hugoniots for water (A; initial temperature of 300 K) and ice (B; initial temperature of 250–263 K) calculated from our Sesame table for H_2O (thick lines) compared to laboratory measured Hugoniots (thin lines) from Stewart and Ahrens (2005). U_s is shock velocity and U_p is particle velocity.

existing hydrocode EOSs for H_2O are inadequate for our needs (e.g., do not include high pressure phases or do not accurately model the melting curve). The table includes three solid phases (ices Ih, VI, and VII), liquid, and vapor. The EOS of the phases and phase boundaries are based on experimental data. The tabulated EOS reproduces measured shock Hugoniots in ice and water (Fig. 2). Calculations using the table are also in good agreement with measured shock and post-shock temperatures of ice by Stewart et al. (2008) and shock temperature data of water (Kormer 1968; Lyzenga et al. 1982). See the appendix for a detailed description of the H_2O table.

Calculations using the tabular EOS assume thermodynamic equilibrium. Shock-induced transformations of ice Ih to ice VI, ice VII and liquid are in excellent agreement with equilibrium phase boundaries, but the Hugoniot elastic limit of ice Ih extends outside of its equilibrium stability field (Stewart and Ahrens 2005). In contrast, many silicate rocks exhibit hysteretic phase transformations under shock loading and unloading (e.g., Sekine et al. 1995; Swegle 1990). CTH allows for mixed cell thermodynamics, which means that each material in a cell can have separate temperatures and pressures. The cell pressure (used to deform the cell) is then the volume fraction weighted average of the material pressures.

Description of Simulations

To investigate the effect of icy layers in the target on the cratering process, we conduct simulations of impacts onto a target with a single icy layer of varying thickness and ice content and at varying depths. The bolide is either a 200 or 1600 m diameter basaltic asteroid (creating a simple and complex crater, respectively) hitting the Martian surface vertically at a velocity of 10 km/s. 10 km/s is slightly lower than the median impact velocity of asteroids on Mars (12.8 km/s) (Bottke et al. 1994), which partially accounts for the fact that most impacts are not vertical (some of the asteroid's energy is partitioned into horizontal movement).

All calculations are initialized with a Martian crust under lithostatic pressure and with a geothermal temperature gradient of 15 K/km, consistent with estimates by Clifford (1993). The pressure and temperature at the surface are assumed to be 6 mbar and 210 K, respectively, to be broadly representative of the present epoch on Mars. No atmosphere is included in this study. We consider surface layers composed of ice, intact basalt, damaged basalt, and sand.

All calculations are conducted in 2D under cylindrical symmetry (exploratory, low resolution 3D runs showed similar results). AMR is used to resolve important parts of the problem without needing to keep the entire mesh highly resolved, which would be computationally expensive. For the 200-m impacts, the projectile is kept resolved to 5 m (40 cells across the projectile diameter), the ejecta blanket and free surface are tracked to a resolution of 10 m, and the shock front was resolved to 20 m. For the 1600 m impacts, the projectile is kept resolved to 40 m (40 cells across the projectile diameter), the ejecta blanket and free surface are tracked to a resolution of 40 m, and the shock front is resolved to 80 m. In all simulations, the icy layers are kept resolved to at least 10 cells across a layer, except for the 200 m diameter impacts with 50 m thick ice layers. In these cases, the ice layers are only resolved to 5 cells across a layer. Finally, massless, Lagrangian tracer particles are used to track the history of parcels of material as they are advected through the Eulerian mesh.

RESULTS

Crater Morphology

A single icy layer significantly modifies cratering mechanics and can result in a range of observable effects on final crater morphology, depending upon the burial depth and thickness of the layer relative to the size of the impactor. Figure 3 presents time series from simulations of a 200 m diameter projectile impacting onto the Martian surface for different target configurations. In Fig. 3a, the target is homogenous basalt. Crater formation proceeds as expected, with the ejecta curtain forming a smooth inverted cone that sweeps outward (20 s) and the formation of a bowl-shaped transient cavity whose walls collapse slightly (200 s). With the addition of a surface ice layer (Fig. 3b and c), formation proceeds as before, but when the basalt ejecta are laid down near the rim, it compresses the ice layer underneath. The compression leads to horizontal, non-ballistic motion of the surface ice layer, which thins the ice near the rim and thickens it at greater distances, leaving the crater with a very indistinct rim. If the thickness of the surface ice layer is large enough (Fig. 3d), then the ice separates from the basalt in the ejecta curtain, and an inner crater (in the underlying basalt) and an outer crater (in the overlying ice) are formed. Similar ejecta curtain structures have been observed in simulations of marine targets (Ormö et al. 2002). Once formed, the icy rim and walls are unstable and flow back into the crater at late times (200 s).

Next, we consider an idealized case of a buried ice layer under an intact basalt layer. Burying the ice layer produces further morphological variations (Fig. 4). A buried ice layer causes the top basalt layer to tear away from the underlying material at early times (2 s). Shock wave reflections between the layers increase the fragmentation of the overlying basalt and modify the ejecta trajectories. The high ejection angles result in a hinge-like evolution of the ejecta curtain. Once formed, the hinge area collapses back towards the crater cavity. As the hinge slumps, it squeezes the ice layer, resulting in a late-stage icy extrusion into the crater. An icy extrusion is seen even in simulations where the ice layer is very thin and shallow relative to the crater size (Fig. 4a). The ice in the extrusion behaves in a fluid manner because it has a low coefficient of friction and because it is warm; however, it is largely unmelted. Note that, in the ice strength model, the coefficient of friction decreases with temperature; at 210 K, it is about 0.3 (low pressure) and 0.1 (high pressure) (see Fig. 1), and at 240 K, it is about 0.1 and 0.05. While these values seem very low, experiments show that with increasing sliding velocity the friction of ice can become extremely small (approaching 0.001 at a sliding velocity of 1 m/s) because of small melt layers that lubricate the ice surfaces (Maeno et al. 2003). Thus, the extrusion can be thought of as a fast moving ice-rich debris flow. When the thickness of the
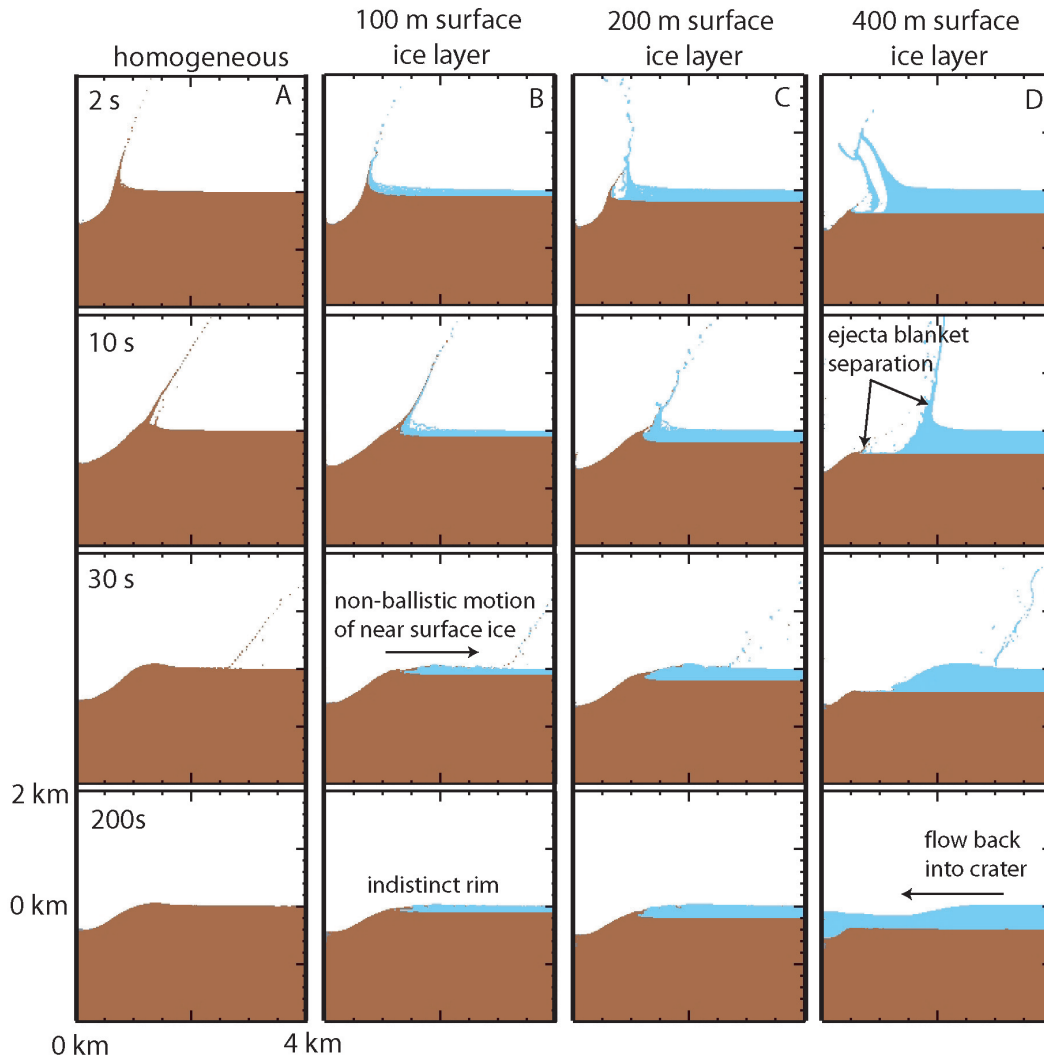
Fig. 3. 200-meter diameter projectile impacting at 10 km/s for different target configurations with a surface ice layer under Martian gravity. Dark color represents basalt and light color represents ice. Time increases downwards and the scale is the same in all panels.

buried icy layer becomes large enough (Figs. 4d and 4e), the actual crater (in the underlying basalt layer) becomes negligible and the amount of ice being extruded into the crater at late times becomes very large. As the ice being extruded from all sides of the crater meets, it creates a central uplift (around 60 s) which later collapses back down in on itself and flows outward.

The physical reason for the observed differences in the cratering process with changing target configuration is a combination of effects from the equation of state mismatch between ice and basalt and the low strength of ice. The equation of state contrast between ice and basalt leads to shock wave reflections between layers, which produces variations in the pressure, particle velocity, and temperature structure in the target. The particle velocity field produced by the shock wave and the strength of the materials controls the excavation flow field that produces the crater. Figure 5 and Fig. 6 illustrate how the peak pressures and temperatures

change with the presence of an icy layer (plots are constructed from tracer particle histories); the ice is shocked to lower pressures relative to the basalt, but undergoes more heating. Note that the temperatures shown are peak shock temperatures and do not correspond to the zone of melting; post-shock temperatures are much lower. In general, incipient melting of ice will begin when the shock pressure reaches 1 GPa, and complete melting will occur when the shock pressure reaches 2.9 GPa (for ambient Martian conditions of about 200 K and 6 mbar). The shock wave reflections between layers also increase fragmentation in the ejecta curtain. The very low strength of ice heated to near the melting point causes late stage flows into the crater cavity and enhances collapse of the transient crater.

The assumption of alternating intact ice and basalt layers is oversimplified; however, these simulations illustrate the range of possible outcomes of cratering into a target with icy layers. In reality, for the cases with a buried ice layer, the
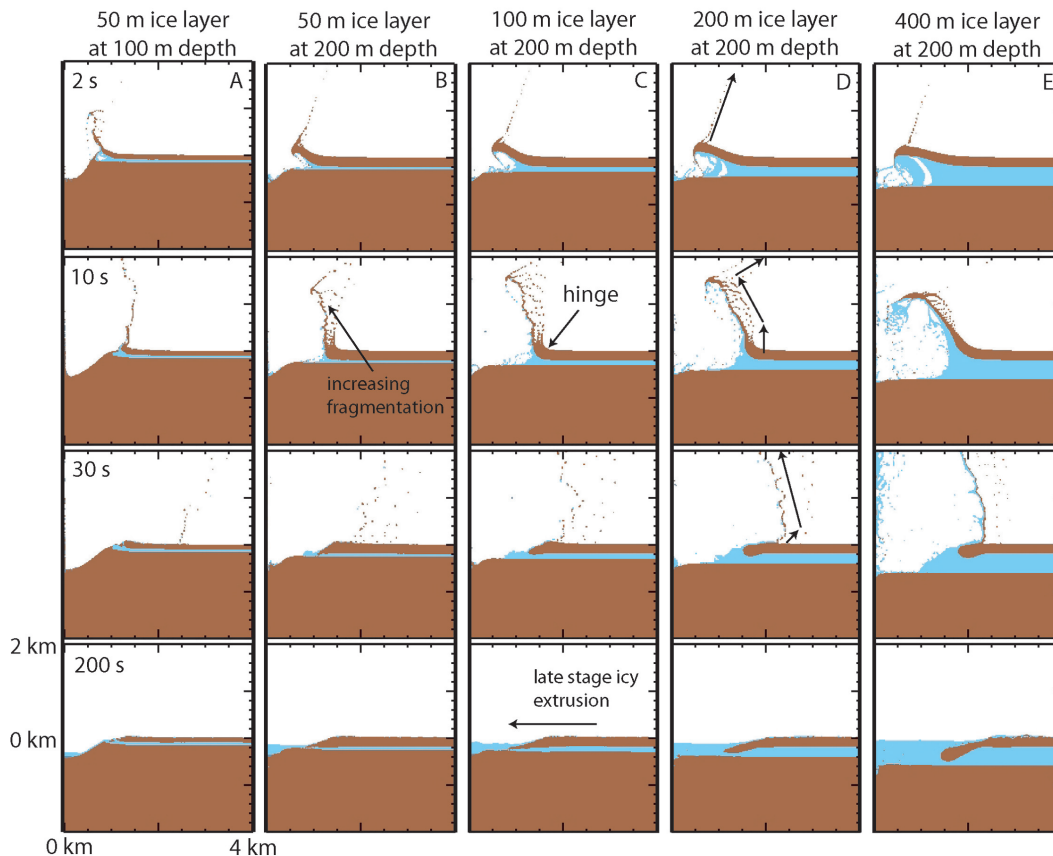
Fig. 4. 200-meter diameter projectile impacting at 10 km/s for different target configurations with a buried ice layer under Martian gravity. Dark color represents basalt and light color represents ice. Time increases downwards and the scale is the same in all panels. Arrows in column D show the ejecta blanket angles.
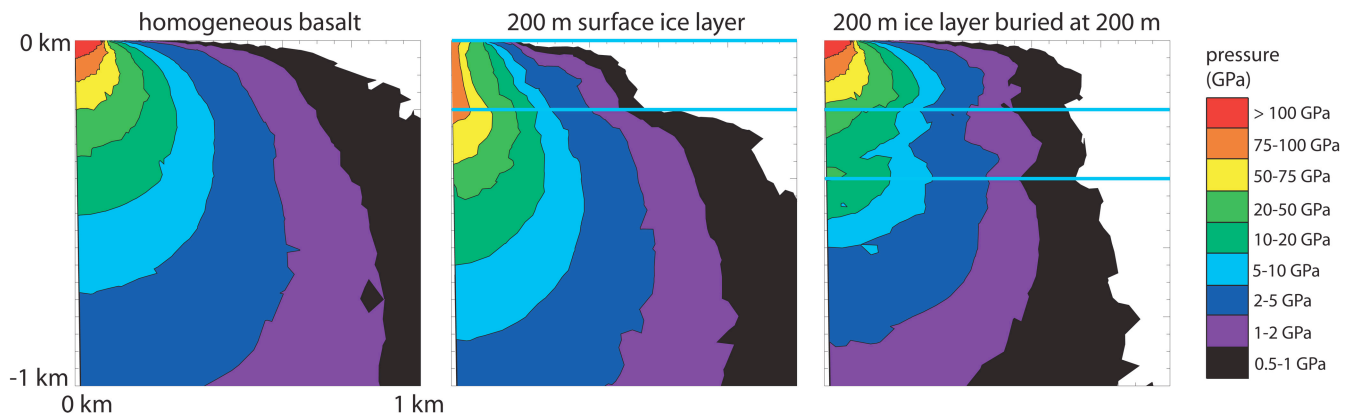

Fig. 5. Peak shock pressures as a function of initial position for a 200 m diameter projectile impacting at 10 km/s into different target configurations under Martian gravity. Horizontal lines show the initial location of ice layers.

overlying basalt is likely to be a heavily fractured regolith or sand deposit. Hence, we also conduct impact simulations where we initialize the upper layer as completely fragmented (using the basalt strength model with damage equal to one) sand. The same general phenomena are observed with a sand surface layer (including modified ejecta trajectories and a late stage icy extrusion) as when the overlying layer is intact basalt. These simulations suggest that the general results from the idealized model cases may be applied to the more complicated layered structures expected on Mars.

An additional complication is that the icy layers are not likely to be pure ice, but to be some mixture of ice and rock. Simulations with varying ratios of ice and rock in the icy layer (Fig. 7) show that, as expected, the effects diminish with decreasing ice volume fraction. The mixture simulations were initialized so that each cell in the icy layer contained both ice
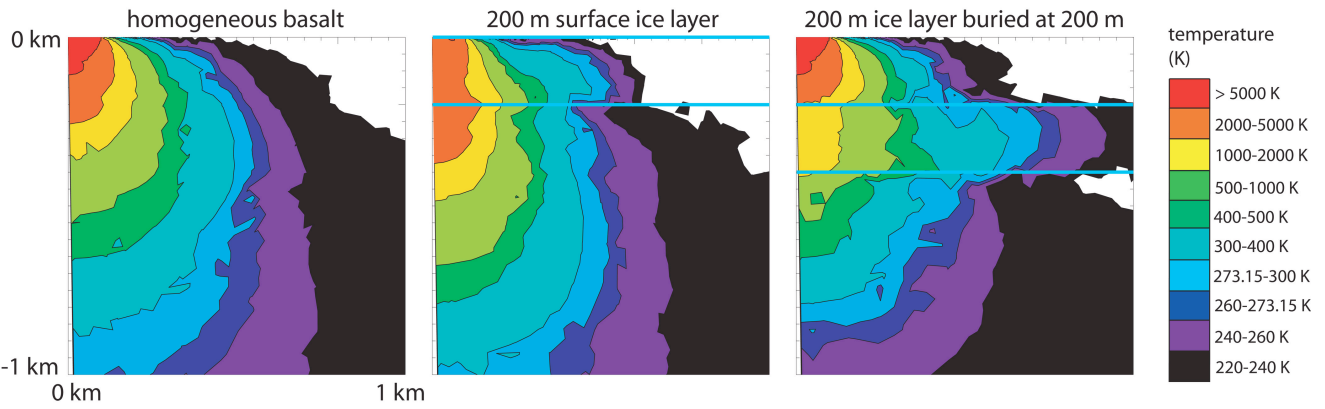
Fig. 6. Peak shock temperatures as a function of initial position for a 200 m diameter projectile impacting at 10 km/s into different target configurations under Martian gravity. Horizontal lines show the initial location of ice layers.
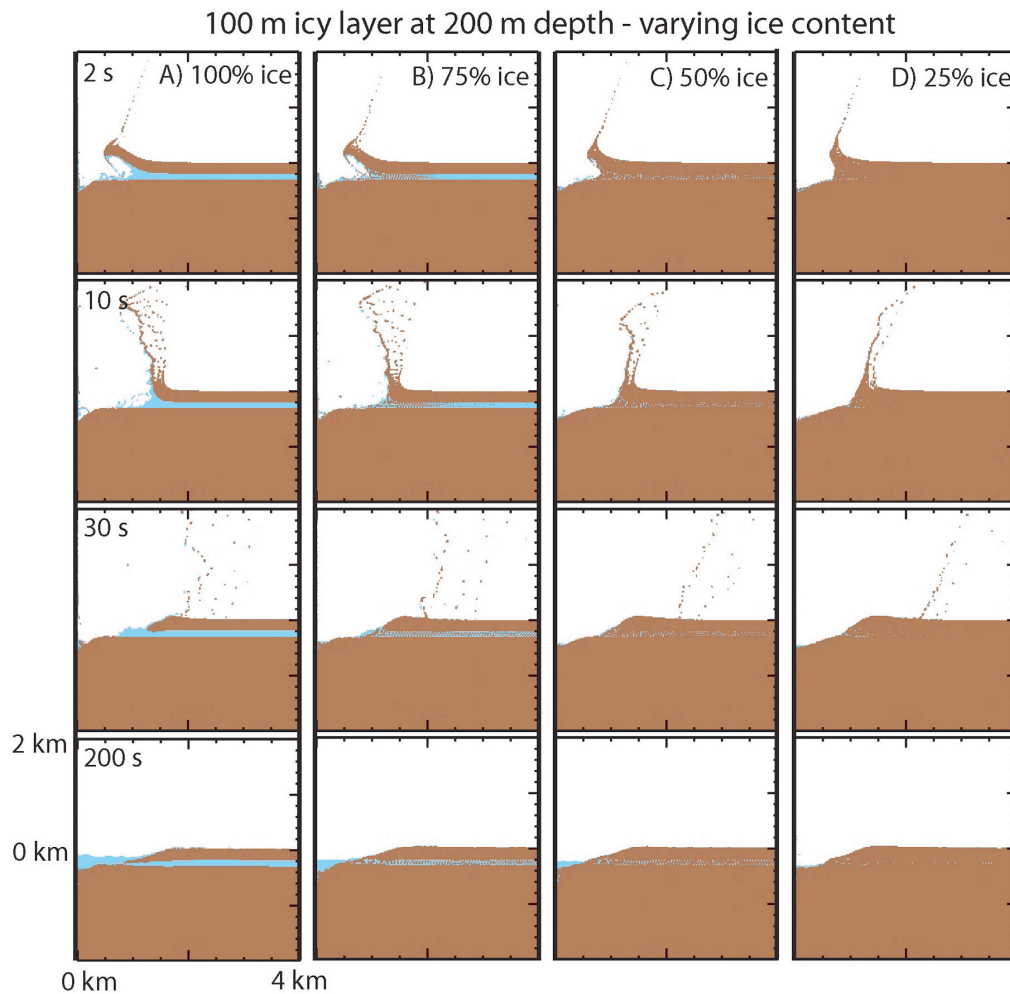

Fig. 7. 200 m diameter projectile impacting at 10 km/s for a 100 m buried icy layer of varying ice content (% volume) under Martian gravity. Dark color represents basalt and light color represents ice. Time increases downwards and the scale is the same in all panels. In these simulations, the ice and rock in the icy layer and the overlying rock are assumed to be completely fractured (damage equal to one).

and rock. Note that even relatively small amounts of ice produce observable effects. Significant crater infilling (late stage icy extrusion) is seen up to about 50% ice volume fraction, and simulations with only 25% ice (Fig. 7d) still display high ejecta angles, an increasing level of fragmentation of the ejecta blanket, and a slump terrace resulting from enhanced crater collapse.

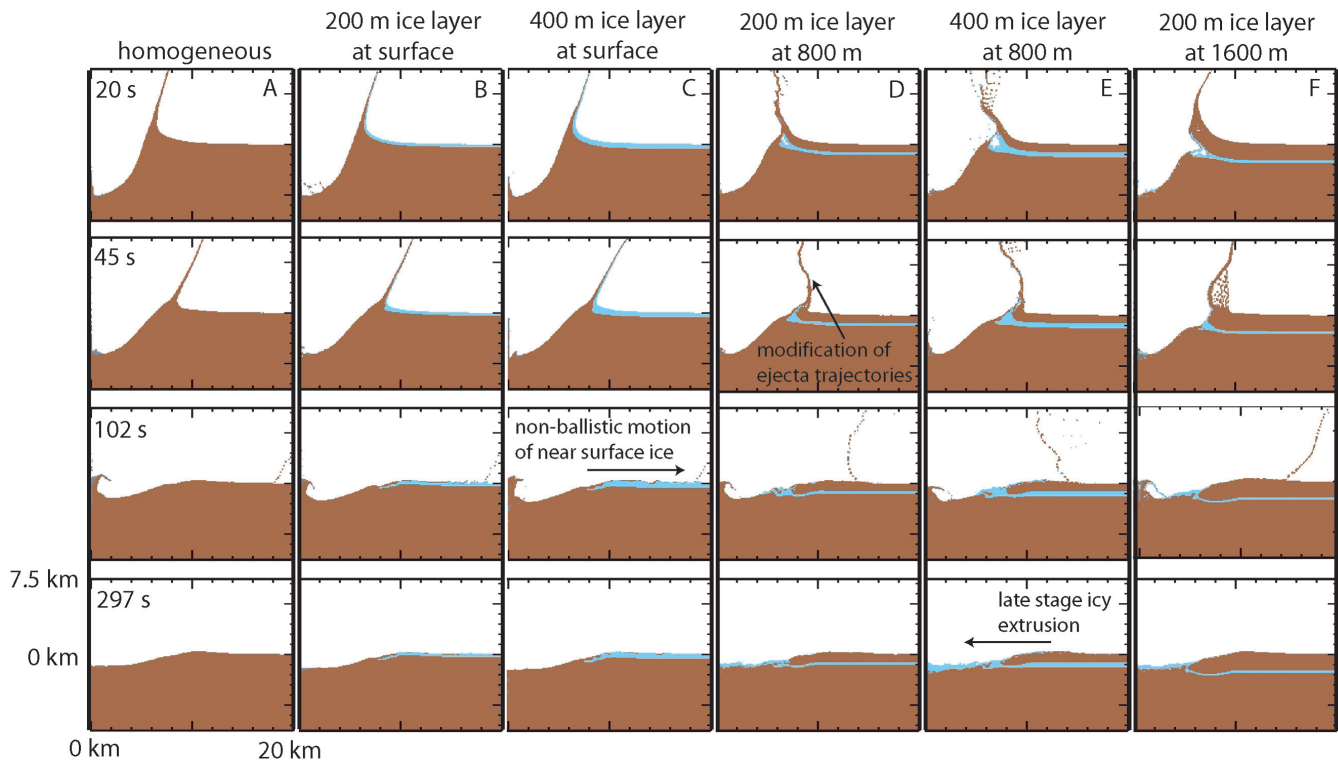Simulations of the formation of a larger crater in an icy

Fig. 8. 1600 m diameter projectile impacting at 10 km/s for different target configurations with a surface and buried ice layer under Martian gravity. Dark color represents basalt and light color represents ice. Time increases downwards and the scale is the same in all panels.

layered target (Fig. 8; 1600-m diameter projectile) produce results similar to those seen for the smaller crater. The magnitude of the observable effects depend upon the thickness and burial depth of the ice layer relative to the crater size, so that an ice layer must be thicker and deeper for a larger crater to produce similar features as around a smaller crater. If a buried ice layer is thin and near enough the surface (not shown), it will be completely folded over into the rim and behave more like the thin surface ice scenarios shown in Fig. 3b than the buried ice scenarios shown in Fig. 4. Around the ~20 km diameter complex crater, a surface ice layer leads to non-ballistic motion in the ejecta blanket, and a buried ice layer displays modification of the ejecta trajectories due to wave reflections as well as a late stage icy extrusion from the crater wall into the floor. Because of their increased sensitivity to target physical properties, small simple craters are the most useful probes of near surface structural variations. Observable indicators of subsurface layering are more subtle around large complex craters.

Finally, while the magnitude and type of effects produced by an icy layer will depend upon a number of complex factors (burial depth, thickness, ice content of layer, surrounding material, etc.), in general, we conclude that significant effects (such as late stage icy extrusions) are seen when the thickness of the icy layer is at least 25% of the diameter of the projectile. We did not conduct simulations with thinner layers, so the lower limit of observability may be even smaller. Note that >35% volume ground ice is inferred by Durham et al.

(2008) to explain observed viscous flow features and Mars Odyssey neutron spectrometer results suggest 40–73% (by volume) ground ice in the upper meter at some locations on Mars (Boynton et al. 2002).

Ejecta

Icy layers modify the excavation processes, altering ejecta velocities and trajectories and leading to significant variations in the ejecta blanket morphology. The effects of target structure are illustrated in three example impact scenarios with different layer configurations, shown in Fig. 9. Qualitatively, the ejection angles are steeper when an icy layer is present compared to a homogeneous rock target. Mobilization of a surface ice layer by impacting ejecta is seen in Fig. 9b, in a manner similar to the ballistic sedimentation model (Oberbeck 1975). The trajectories of Lagrangian tracer particles also illustrate the complicated flow path of late stage extrusion into the crater cavity (Fig. 9c).

The magnitude of the changes in the ejection process due to layering is shown quantitatively in Fig. 10. Our simulations demonstrate that the initial launch velocity of ejecta is a function of the target structure. Figure 10a presents the average launch velocity (by volume) of ejecta that is ejected at a given distance from the crater center. These velocities are calculated by back-tracking the ballistic ejecta trajectories from 10 s, and are checked against the launch velocities of tracer particles in the ejecta. There is good agreement
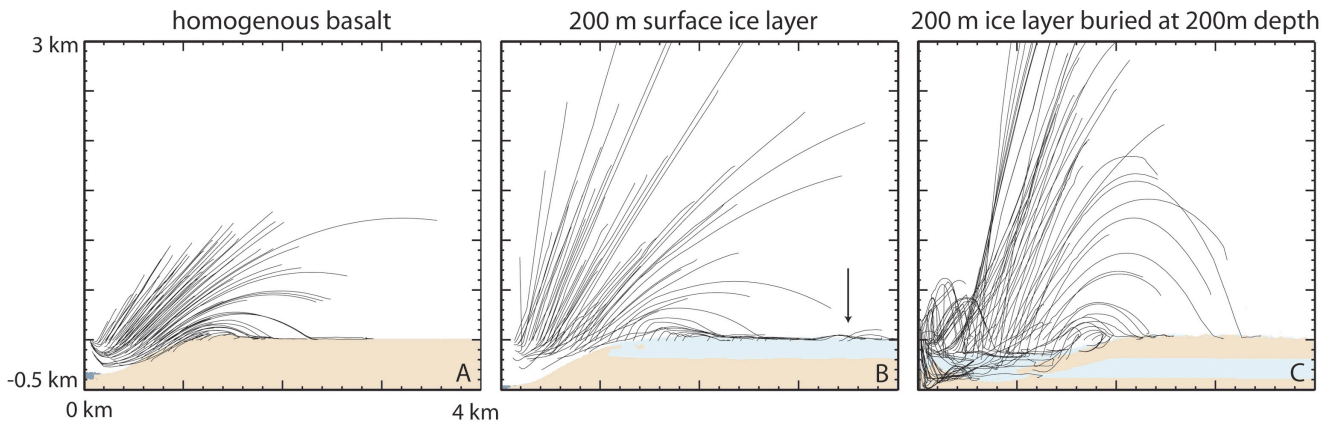
Fig. 9. Example ejecta trajectories, derived from massless, Lagrangian tracer particles, for a 200 m projectile impacting at 10 km/s onto different target layer configurations. Trajectories that end abruptly in the air indicate that the tracer was separated from material during the calculation. Arrow indicates example location of mobilization of surface layer ice by impacting ejecta. The scale is the same in all panels. Case A corresponds to Fig. 3a, B to Fig. 3c, and C to Fig. 4d.
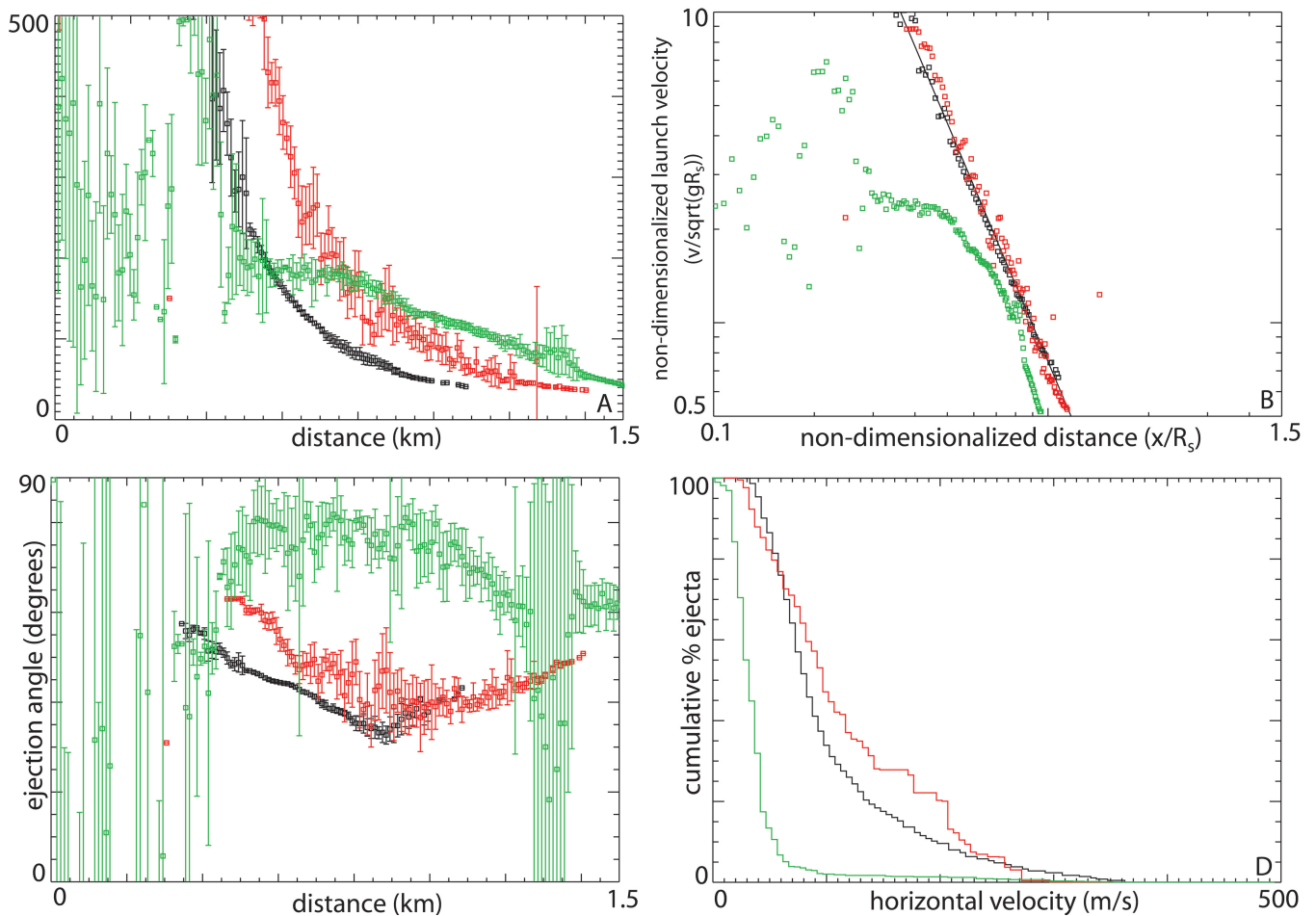

Fig. 10. Selected measures of the ejection process for target configurations shown in Fig. 9: black (dark color)—homogeneous basalt target, red (medium color)—200 m surface ice layer, green (light color)—200 m ice layer buried at a depth of 200 m. a) Average launch velocity (by volume) of ejecta that is ejected versus distance from crater center. b) Non-dimensionalized launch velocity versus non-dimensionalized distance from crater center. c) Average ejection angle versus distance from crater center. d) Cumulative % of ejecta (by volume) greater than a given horizontal velocity. The line in B is the ejecta scaling law for dry sand from Housen and Schmidt (1983) (Equation 1). Error bars represent one standard deviation.

between the two methods. When there is a surface ice layer (red/medium shade points), the launch velocity distribution is very similar to a homogenous rock target (black points), however the distribution is shifted to the right (to greater distances from the crater center). The shift results from the fact that the target is weaker and less dense when an ice layer is included, leading to more ejecta and a larger transient crater radius. Additionally, when there a surface ice layer, the error bars in velocity tend to be larger, indicating that there is a larger spread in the velocities ejected at any given distance. When there is a buried ice layer (green/light points), wave reflections in the target dramatically reduce the launch velocities near the impact point and increase the velocities at greater distances compared to the homogeneous target. Also, in this case, launch velocities near the crater center are highly scattered and do not show any meaningful trend with distance.

Ejecta scaling laws are often used to estimate the velocity distribution in the ejecta curtain. We compare the ejecta launch velocities produced in the simulations to ejecta scaling laws developed from experimental data and dimensional analysis (Housen and Schmidt 1983). In Fig. 10b, the ejection velocity results are replotted in terms of non-dimensionalized launch velocity versus non-dimensionalized distance and compared to the scaling law derived for dry sand (scaling laws for rock are not well constrained) from Housen and Schmidt (1983):

$$\frac{v}{\sqrt{gR_s}} = C\left(\frac{r}{R_s}\right)^{\frac{x-3}{z\alpha}} \qquad (1)$$

In Equation 1, $\frac{v}{\sqrt{gR_s}}$ is the non-dimensionalized launch velocity, $\frac{x}{R_s}$ is the non-dimensionalized distance from the crater center, v is the launch velocity, g is the gravitational acceleration, R_s is the transient crater radius at the pre-impact surface level, r is the distance from the crater center, c and α are experimentally determined constants.

Our simulations with homogenous basalt and a surface ice layer agree well with the scaling law for dry sand. However, the buried ice layer shows a strong departure from a simple power law for $x/R_s < 0.7$. R_s is 1.01 km for homogenous basalt, 1.23 km for the surface ice layer case, and 1.63 km for the buried ice layer case. C is 0.75 (chosen to fit the simulations, since there is little experimental constraints for this constant), and α is 0.49, which is the exponent for dry sand from Housen and Schmidt (1983). Note that changing C and R_s would shift the lines up/down and left/right, but would not affect the slope. These results indicate that great care should be taken when applying power law velocity distributions to interpreting ejecta deposits around craters formed in layered target structures.

As noted above, our simulations show that ejecta launch angles are also a function of target structure (Fig. 10c). In general, adding a surface ice layer does not change the average launch angle of ejecta with distance; both scenarios show ejection angles ranging from about 60 to 30 degrees (with the angle decreasing with distance). However, adding a buried ice layer leads to much higher ejecta angles (around 70–80 degrees). The change in ejection angle is clearly seen in Fig. 9. In the buried layer case (Fig. 9c), some of the ejecta is thrown out at such high angles that the trajectories land within the final crater rim, slumping back into the crater at late times. The lower launch velocities coupled with the higher ejection angles in the buried ice layer case lead to cumulatively much lower horizontal velocity components for the ejecta compared to the other two cases (Fig. 10d). In Fig. 10d, the cumulative horizontal velocity volume distributions are shown for all of the ejected material, including material that ultimately resides in the final crater cavity.

The changes in ejecta velocities and trajectories with target properties lead to variations in the structure of the resulting ejecta curtain, particularly for the case of a buried ice layer. For the surface ice scenario, the ejecta curtain shows a very similar structure to a homogenous target (compare Figs. 3a and c). An observable difference is the thicker and "rougher" ejecta curtain in the surface ice layer case, compared to the straighter, thinner ejecta curtain in the homogenous target case. The difference is a result of the greater spread in launch velocities (larger error bars). For the buried ice scenario, there are two kinks in the ejecta curtain (Figs. 4d, 10 s). These kinks lead to three segments of the ejecta blanket, with the middle segment actually having an inverted form (angled inward as opposed to outward) from what is usually seen in cratering studies. The presence or absence of this inverted form is very sensitive to the exact target structure (thickness and burial depth of the icy layer), suggesting that observable features may provide reasonable constraints on subsurface structure. For example, in Fig. 8e the ejecta curtain structure is similar to in Fig. 4d, but in Fig. 8f, an inverted segment is not seen.

The ultimate result of these differences in the ejection process is observable changes in the ejecta blanket profile (Fig. 11). The initial ejecta thickness plots are constructed by looping through all of the computational cells containing ejecta when transient crater formation is complete (10 s) and calculating the range assuming a ballistic trajectory from this point forward. The dashed lines in Fig. 11 show the power law ejecta thickness distribution from McGetchin et al. (1973), which is based on an analysis of simple terrestrial explosion craters:

$$\delta = 0.14 R_R^{0.74}\left(\frac{r}{R_R}\right)^{-3.0}, \qquad (2)$$

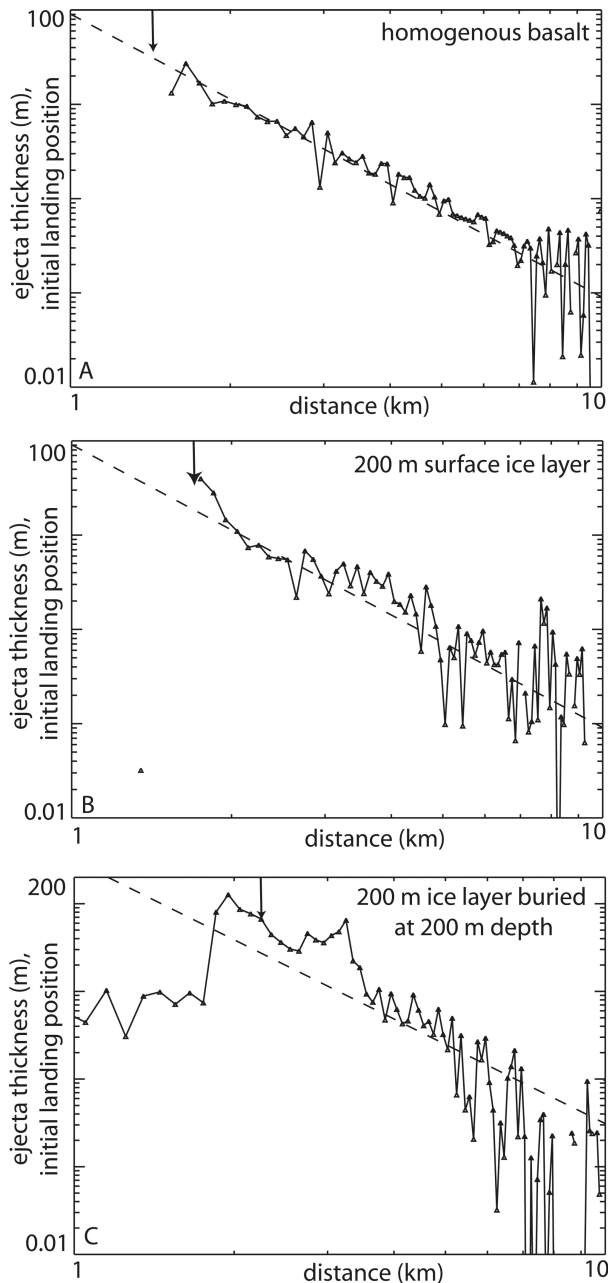where δ is the ejecta blanket thickness, r is the distance

Fig. 11. Initial ejecta blanket thicknesses versus distance from crater center for simulations shown in Fig. 9. Arrows show the approximate locations of the final crater rims. The dashed lines show the experimental ejecta thickness distribution from McGetchin et al. (1973). Note that the ejecta blanket thicknesses are based on the initial landing position and do not account for any subsequent horizontal movement and incorporation of secondary materials.

from the crater center, and R_R is the rim-to-rim transient crater radius (1.44 km for the homogenous basalt and 200 m surface ice layer cases and 2.0 km for the 200 m buried ice layer case).

When the target is homogeneous (Fig. 11a), the ejecta thickness follows a relatively smooth power-law with a slope

of about −3.0, as expected. Adding a surface ice layer does not significantly change this shape (Fig. 11b), while adding a buried ice layer produces dramatic variations (Fig. 11c). These results are a direct reflection of the fact that a buried ice layer results in material being ejected at higher angles and lower velocities, which leads to the majority of the ejecta falling very close to the crater. Quantitatively, 90.6% of the ejecta lie within 5 km of the crater center, compared with 70.6% when there is no ice layer. Notably, there is a steep drop off in the ejecta thickness at a distance of about 3.5 km in the buried ice scenario (at about 1.5 rim radii from crater center, see section Ejecta Blanket Variations).

It is important to note that the method for calculating ejecta thickness provides only the initial landing position of the ejecta and does not include any subsequent horizontal, non-ballistic motion. The amount of horizontal motion cannot be constrained by the current model due to a lack of resolution (at the scale of the flow) and inclusion of the appropriate physics (the physics of debris flows). However, studies have shown that Martian ejecta flows are generally less efficient than volatile-rich flows on Earth, and behave more like terrestrial dry volcanic rock avalanches (Barnouin-Jha and Buczkowski 2007). For the buried ice layer scenario, the ejecta in the thick inner region within 3.5 km has horizontal velocities <50 m/s. We suggest that it is unlikely that this feature is completely wiped out by subsequent horizontal flows. Finally, we also note that the finest ejecta fraction may be further modified by interactions with the atmosphere (Barnouin-Jha and Shultz 1998, 1999; Schultz 1992).

DISCUSSION

Comparison with Observations

We have shown that icy layers modify the cratering process and lead to significant and observable effects on the final crater and ejecta morphology. In this section, we compare the simulation results to observations of Martian craters and discuss the implications.

Natural Variations in Crater Dimensions

Our simulations show that fresh craters on Mars can display a range of morphologies, which has important implications for cratering studies. The geometries of well preserved craters have been used to infer a plethora of information about a planet, including regolith thicknesses (e.g., Oberbeck and Quaide 1967; Quaide and Oberbeck 1968), strengths (e.g., Stewart and Valiant 2006), amounts and rates of degradation and infilling (e.g., Forsberg-Taylor et al. 2004), and the presence of possible crater lakes (e.g., Cabrol and Grin 1999). Comparisons of fresh crater forms between planets has been used to infer mechanisms of formation and collapse (e.g., Pike 1988). Such studies require that the shape of a fresh crater be known; however, this is
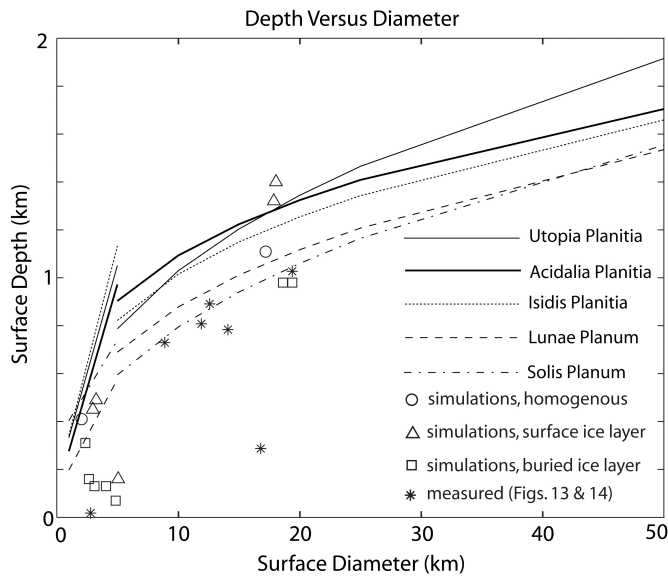
Fig. 12. Depth versus diameter measured at the pre-existing surface level for simulations in Figs. 3, 4, and 8 (circles, triangles and squares) compared with measurements by Stewart and Valiant (2006) of fresh craters in different regions on Mars (lines). Also shown are measurements of the craters shown in Figs. 13 and 14 (asterisks).

often difficult. Most studies make assumptions about what the freshest shape is (often assuming that the deepest craters are the freshest) and check these craters for visual clues of erosion. However, our results show that the deepest craters are not necessarily the most pristine.

Figure 12 compares the simulation depth versus diameter results to measurements of the deepest Martian craters by Stewart and Valiant (2006). The cases with a surface ice layer (triangles) tend to produce craters that are slightly deeper than in the homogenous case (circles) (the exception is the simulation shown in Fig. 3d, because the ice layer is large enough relative to the crater that it is unstable and flows back into the crater). The increased depth is due to the projectile penetrating deeper through the lower density ice than it would in a pure basalt target, effectively increasing the burial depth of the impact energy. Conversely, buried ice layers (squares) tend to produce craters that are shallower than expected, due to late stage infilling by extruding ice during crater collapse. Thus, a crater may be fresh and much shallower than nearby fresh, deeper craters if spatial or temporal variations of subsurface volatile content exist within a region. Using a depth cut-off criterion to identify fresh craters will mistakenly omit some craters. The problem can be mitigated by choosing small regions (minimizing spatial target variations), although doing so will then lead to problems with small numbers (not having enough fresh craters).

Attempts have been made to define a global pristine crater population on Mars by choosing the deepest craters over the entire planet (Boyce and Garbeil 2007). However, it

is unlikely that such a function exits, because the amount of surface and subsurface ice varies widely over the planet and changes with time. The variation in ice content will cause fresh crater morphologies to vary both spatially and temporally.

Furthermore, our results show that not only are the freshest craters not necessarily the deepest, but the strongest material is also not necessarily the deepest either: the simulations with a weak surface layer of ice produced deeper craters. Thus, it is very difficult to interpret the observed regional variations in fresh Martian craters in terms of a single measure of strength (Boyce et al. 2006; Stewart and Valiant 2006).

Infilled Craters

Low and mid-latitude shallow, infilled Martian craters (such as those shown in Fig. 13) are generally assumed to have undergone secondary modification processes, such as aeolian or lacustrine deposition (e.g., Craddock et al. 1997; Cabrol and Grin 1999; Boyce et al. 2004, 2005; Forsberg-Taylor et al. 2004), and their presence has been used to infer a past ocean in the Northern plains (Boyce et al. 2005). However, our simulations show that some of the infilling and shallowing may be a primary process, resulting from the late stage icy extrusion of a buried icy layer into the crater. Primary infilling during cratering may be particularly relevant for infilled craters where the ejecta blanket is still relatively pristine, as it is difficult to imagine an aeolian or lacustrine process that is able to extensively infill the crater without significantly eroding the ejecta blanket. Examples of partially infilled craters with relatively well-preserved ejecta blankets are shown in Fig. 13, and their depths and diameters are plotted on Fig. 12, where it can be seen that the example craters range from slightly shallower than normal to almost completely infilled.

An alternative explanation for these shallow craters is viscous relaxation, such as has been used to explain the morphologies of craters on Mars' polar layered deposits (Pathare et al. 2005). However, the polar craters are formed entirely in an icy layer, whereas the ice layer in these scenarios makes up a much smaller portion of the target, limiting relaxation rates. Another possible explanation is that the craters and ejecta were covered by icy deposits during a glacial cycle. As the icy deposits were later eroded/sublimated, the crater and ejecta was exposed but some of the infilling was preserved. This process has been suggested to explain excess ejecta around some high latitude craters (Krevslavsky and Head 2006). In contrast, close examination of some mid-latitude craters with excess ejecta suggest that they formed in the presence of a pre-existing near-surface icy layer (Barlow and Perez 2003; Black and Stewart 2008; Meresse et al. 2006), which could lead to infilling during crater collapse.
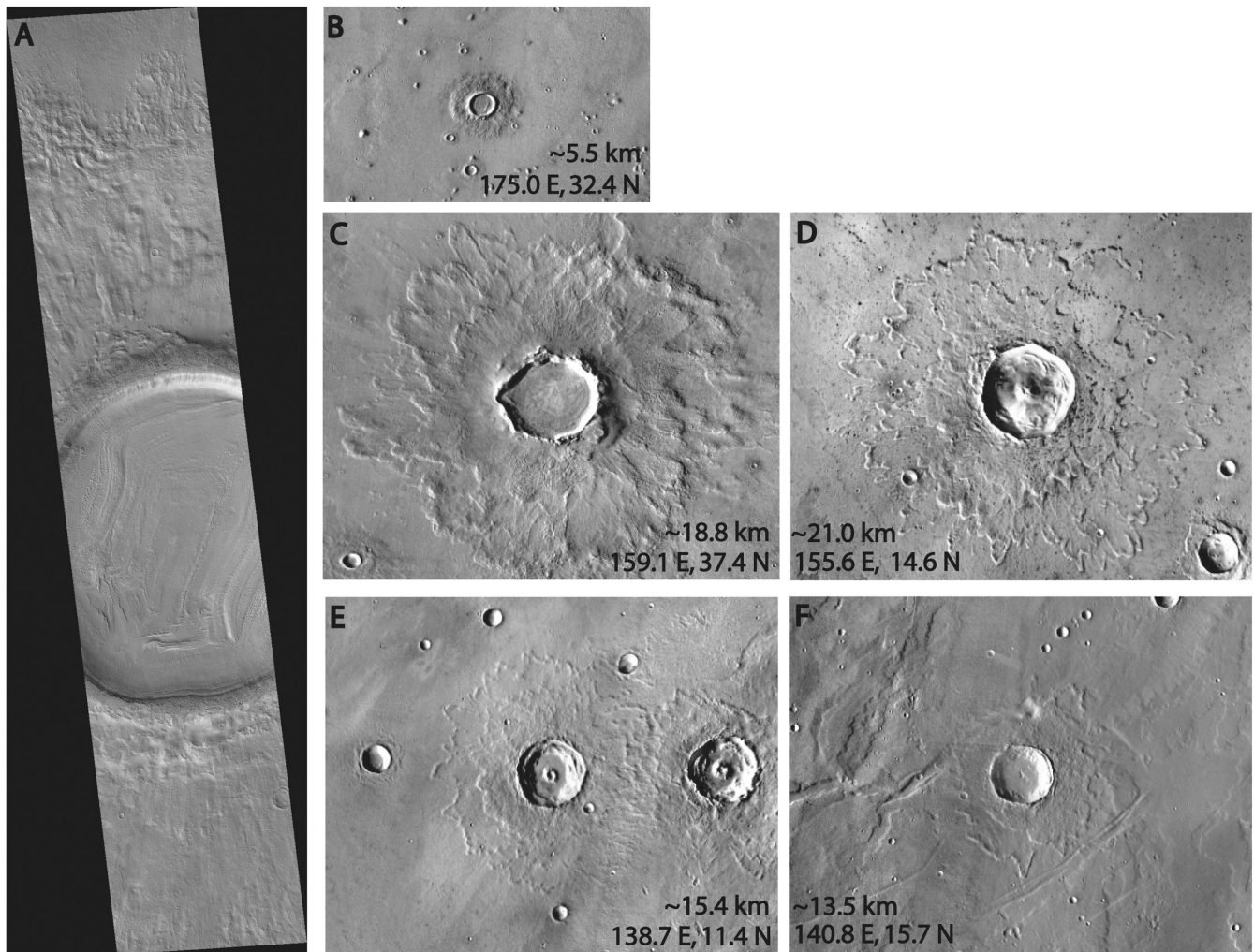
Fig. 13. Examples of infilled craters on Mars at low and mid-latitudes. Location (latitude and longitude) and approximate crater diameters (rim-to-rim) are given in the corners of the figures. Note that A and B are two views of the same crater. A is MOC (Mars Orbiter Camera) release number MOC2-674 (NASA/JPL/Malin Space Science Systems), while B through F are THEMIS images from JMARS (http://jmars.asu.edu). A/B and C are on the western edge of Amazonis Planitia, northeast of Elysium Mons, and D, E, and F are just south of Elysium Mons.

"Dewatering" Features

Recently, High Resolution Imaging Science Experiment (HiRISE) images have been used to identify and document flow features (channels, alluvial fans, ponded material) associated with young impact craters of a large size range (~3 to 60 km) (Mouginis-Mark et al. 2007; Tornabene et al. 2007a, 2007b). Some of these features are interpreted to be wet or icy debris flows, such as the example shown in Fig. 14d (Mouginis-Mark et al. 2007; Tornabene et al. 2007a, 2007b). The debris flows appear on steep slopes, such as around the central uplift, and on the wall, rim and ejecta. Our results suggest that some of these features may be created by icy material flowing inward as a late stage icy extrusion (buried ice layer case). Such flows may also help to carve channels through which water can later flow, possibly contributing to the formation of the gullies that are seen along many crater walls. Even a thin, relatively low volatile content (50%) icy layer extrudes a small amount of icy material (Fig. 4a), suggesting that debris flow features should be widespread (as observed). Additionally, HIRISE images of crater interiors has revealed ponded material with a pitted texture that are interpreted as deflated devolatilized materials; an example is shown in Fig. 14a (Mouginis-Mark et al. 2007; Tornabene et al. 2007a; Tornabene et al. 2007b). These features could represent devolatilization of a warm, late stage icy extrusion. Also note that devolatilization has been proposed to explain the formation of central pits (Barlow 2006).

Crater Lakes and Hydrothermal Systems

Ponded ice at the bottom of a crater (such as is produced for our simulations with a buried ice layer) may have implications for the formation of crater lakes and
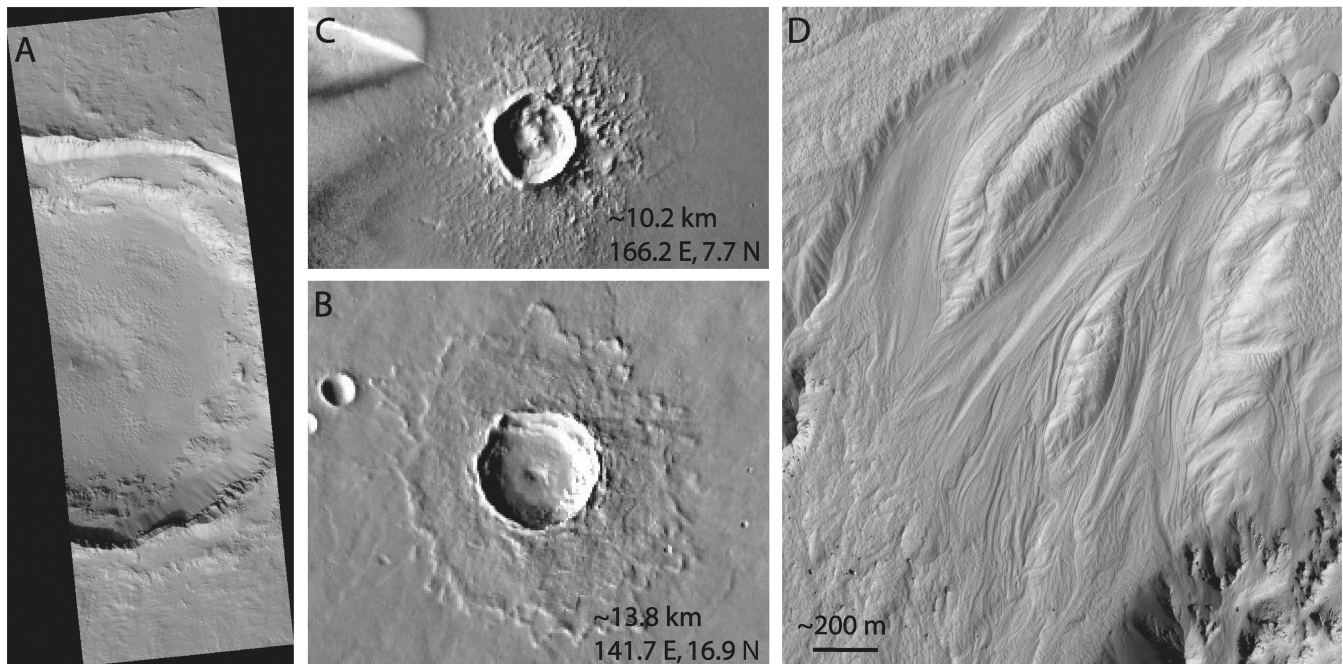
Fig. 14. Examples of craters with "dewatering" features. A. Pitted material on the floor of an unnamed crater. Image is HiRISE subimage PSP_004244_1970 (NASA/JPL/The University of Arizona). B. Context image for A. C. Context image for D. D. Wet debris flow around the central uplift of Zunil crater. Image is HiRISE subimage PSP_001764_1880 (NASA/JPL/University of Arizona). B and C are THEMIS images from JMARS (http://jmars.asu.edu).
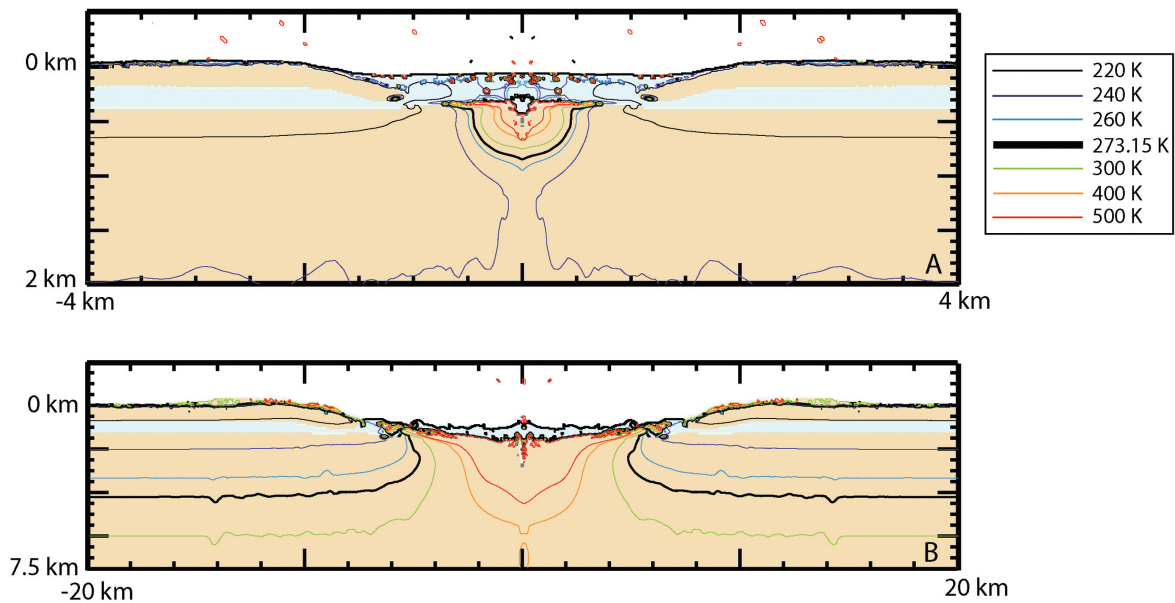

Fig. 15. Final temperature contours beneath craters formed by (A) a 200 m diameter projectile impacting at 10 km/s into a target with a 200 m thick ice layer buried at 200 m depth (Fig. 4D) and (B) a 1600-m diameter projectile impacting at 10 km/s into a target with a 400 m thick ice layer buried at 800 m depth (Fig. 8E).

hydrothermal systems. For the crater sizes calculated here, the ponded ice is heated but not melted, and some of the water in the ejecta blanket is melted. Figure 15a shows that for the 200 m impactor case, the majority of the ponded ice is between 220 and 260 K, with discrete small volumes of hotter ejecta. For

the 1600 m impactor case (Fig. 15b) the ice is even hotter: it is right below the melting point, between 272 and 273 K (for an even larger crater, the ice should be melted and/or vaporized). However, directly under the ice in both cases is a warm core of heated rock (>500 K) that originally lined the

transient crater cavity. Note also that these are relatively small craters; larger craters will have greater amounts of heated rock beneath the crater floor. Conduction of this heat may lead to melting and create a crater lake (Cabrol and Grin 1999). Additionally, it has been suggested that craters provide ideal locations for the development of hydrothermal systems on Mars as a result of the heating produced by the impact (e.g., Kring 2003; Abramov and Kring 2005; e.g., Newsom et al. 2001; Rathbun and Squyres 2002; Pierazzo et al. 2005). Calculations show that the presence of a crater lake in the hydrothermal system will increase the amount of circulation but decrease the lifetime of the system (Abramov and Kring 2005).

Ejecta Blanket Variations

Icy layers may explain some of the variations seen in the ejecta blankets around Martian craters. Martian ejecta blankets display profiles that are different from those seen around lunar craters and include "fluidized" (appearing) layers (SLE—single layer ejecta, DLE—double layer ejecta, and MLE—multiple layer ejecta) as well as distal scarps or ramparts (Barlow et al. 2000). The inner layer in DLE type craters is observed to be much thicker than the outer layer by 10s to 100s of meters (Black and Stewart 2008; Boyce and Mouginis-Mark 2006). We show that icy layers can produce changes in the ejecta blanket structure that modify the radial distribution of ejecta from a simple power law. It is possible that buried icy layers may (if the thickness, burial depth, and ice content are in an appropriate range) produce many of the features seen by DLE type ejecta. Analysis of the ejecta around a simple crater produced in a target with a 200 m ice layer buried at 200 m depth (Fig. 11c) shows that the ejecta blanket can be divided into two distinct segments: a thicker inner region with a steep drop off (at ~3.5 km) to a thinner outer region, which may correspond to the two layers seen in DLE ejecta. Additionally, Boyce and Mouginis-Mark (2006) observe a deficit of secondary craters around DLE craters. Our simulations show that when there is a buried ice layer, the ejecta flow is altered, leading to most of the ejecta being deposited very close to the crater rim. This close deposition may result in a relative deficit of secondaries. Note that the example buried layer case in Fig. 11c considered a pure ice layer. More detailed comparisons to observed crater profiles require modeling a range of ice-rock mixtures. Also if buried ice layers are associated with DLE craters, then the concentration of DLE craters in the 45–65 °N and S latitude ranges (Barlow 2005; Barlow and Bradley 1990) suggests significant amounts of buried ice there at depths greater than observed by Mars Odyssey. The craters that display DLE morphology in this region are generally much larger (diameter up to 50 km) than the buried ice simulation discussed (diameter approximately 4 km), suggesting that a possible ice layer must be much deeper and thicker than in the example simulation. Additionally, horizontal motion of icy

material after deposition of the initial ejecta blanket (not included in the ejecta profiles shown in Fig. 11, but can be seen when looking at tracer history profiles in Fig. 9) will further modify the ejecta distribution.

Icy Layers versus Weak Layers

To use crater morphology to decipher climate history, it is important to be able to differentiate between the effects of icy layers versus non-icy weak layers (such as sediments). Hence, we also simulated impacts into layers of strong and weak basalt (using the ice strength parameters for the weak rock layer). We find that the ice strength model is an important factor. Equally weak icy and non-icy layers exhibit similar effects. Both types of layers modify the excavation and collapse process, producing variations in rim heights, depths, and ejecta blanket morphologies. However, the strength of ice is much lower than the strength of non-icy weak rocky materials. For example, dry sediment has a coefficient of friction of about 0.6, while ice has a coefficient of friction of about 0.2 or lower. Thus, the effects of icy layers will be much more dramatic than weak sediments. In addition, weak layers will not be able to form fluvial features such as late stage infilling and associated "dewatering" features, crater lakes, and infilled craters. We show that when there is an icy layer, some of the ice that infills the crater is very close to its melting point and sitting directly atop heated rock. Thus, devolatilization features are also expected. Generally, icy layers may be less dense than rocky layers, which also influences the burial depth of the impact energy and the ejection process. Hence, although extremely weak rocky layers may produce a portion of the observable effects in this work, we find that weak rocky layers cannot explain all of the observed features associated with Martian impact craters. Given that ice is known to be present on and near the surface of Mars, it is extremely plausible that some layers are weak because they are icy.

Glacial-Interglacial Cycles

The introduction outlined how recent work has led to the theory that ice is deposited at lower latitudes during periods of high obliquity (glacial cycles) and is then sublimated and transported back to the poles at periods of lower obliquity (interglacial cycles). Depending on the time scales involved and the rate of sublimation, ice may remain between glacial cycles and build up, with varying amounts of dust being deposited over the icy layers during interglacial periods (e.g., Milliken et al. 2003). Thus, during a glacial cycle, when ice is present on the surface at lower latitudes, small fresh craters should largely display surface ice morphologies. During an interglacial period, ice may become buried at some shallow depth, and small fresh craters may display a mix of surface ice and buried ice morphologies (depending on the burial depth,

amount of ice, etc.). It is harder to predict the morphologies of larger craters, which are less sensitive to small scale changes in the target structure, and are more dependent on the deeper surface.

Here, we suggest that many of the anomalous features associated with Martian craters, including infilled craters with well-preserved ejecta blankets, "dewatering" features, crater lakes, and variations in ejecta blanket morphologies, may be a result of icy layers. The common occurrence of these features at low- and mid- latitudes supports the theory that glacial periods can lead to the buildup of ice at these latitudes. In the future, studies of crater forms could be used to investigate the climate history (where ice was deposited during glacial periods, estimates of layer thicknesses, etc.) and crustal properties of Mars in more detail.

Conclusions

We present calculations of crater formation under Martian conditions with near-surface icy layers. The low strength of ice at Martian surface temperatures and the shock impedance contrast between icy and rock layers couple to significantly modify the cratering mechanics. For example, a surface ice layer can result in non-ballistic flow of near surface ice and indistinct rims, while a buried ice layer can result in ejecta blanket variations and a late stage icy extrusion into the crater floor. In addition, the presence of an icy layer modifies the velocities, angles, and volumes of ejecta, leading to deviations of initial ejecta blanket thickness from a smooth power law. The modification of the excavation and collapse process significantly changes the final crater morphology, producing observable features which may explain some of the unique aspects of Martian impact craters, including variations in morphometry, shallow craters with pristine ejecta blankets, and "dewatering" features.

The target layer composition and geometries investigated in this paper are simplified representations of the near-surface crust on Mars. While this work has demonstrated a wide range of observable features resulting from ice-rich layers, more detailed studies and observational constraints are needed to concretely link the modeling and observations and confirm the inferences drawn here. In summary, we infer that the cratering record preserves the complex climatic history of Mars by probing the locations, amounts, and temporal variations of surface and subsurface icy layers, but future cratering studies will be needed to decipher the details of this complex and rich record.

Editorial Handling—Dr. Elisabetta Pierazzo

REFERENCES

Abramov O. and Kring D. A. 2005. Impact-induced hydrothermal activity on early Mars. *Journal of Geophysical Research* 110(E12), doi:10.1029/2005JE002453.

Arakawa M. and Maeno N. 1997. Mechanical strength of polycrystalline ice under uniaxial compression. *Cold Regions Science and Technology* 26:215–229.

Barlow N. G. 2005. A review of Martian impact crater ejecta structures and their implications for target properties. GSA Special Paper 384. Boulder: Geological Society of America. pp. 433–442.

Barlow N. G. 2006. Impact craters in the northern hemisphere of Mars: Layered ejecta and central pit characteristics. *Meteoritics & Planetary Science* 41:1425–1436.

Barlow N. G., Boyce J. M., Costard F. M., Craddock R. A., Garvin J. B., Sakimoto S. E. H., Kuzmin R. O., Roddy D. J., and Soderblom L. A. 2000. Standardizing the nomenclature of Martian impact crater ejecta morphologies. *Journal of Geophysical Research* 105(E11):26,733–26,738.

Barlow N. G. and Bradley T. L. 1990. Martian impact craters: Correlations of ejecta and interior morphologies with diameter, latitude, and terrain. *Icarus* 87:156–179.

Barlow N. G. and Perez C. B. 2003. Martian impact crater ejecta morphologies as indicators of the distribution of subsurface volatiles. *Journal of Geophysical Research* 108(E8), doi:10.1029/2002JE002036.

Barnouin-Jha O. S. and Buczkowski D. L. 2007. Comparing the runout of fluidized ejecta on Mars with mass movements on Earth (abstract #1304). 38th Lunar and Planetary Science Conference. CD-ROM.

Barnouin-Jha O. S. and Shultz P. H. 1998. Lobateness of impact ejecta deposits from atmospheric interactions. *Journal of Geophysical Research* 103 (E11):25,739–25,756.

Barnouin-Jha O. S. and Shultz P. H. 1999. Interaction between an impact generated ejecta curtain and an atmosphere. *Journal of Impact Engineering* 23:51–62.

Beeman M., Durham W. B., and Kirby S. H. 1988. Friction of ice. *Journal of Geophysical Research* 93 (B7):7625–7633.

Belton M. J., Thomas P., Veverka J., Schultz P., A'Hearn M. F., Feaga L., Farnham T., Groussin O., Li J., Lisse C., McFadden L., Sunshine J., Meech K., Delamere W. A., and Kissel J. 2007. The internal structure of Jupiter family cometary nuclei from deep impact observations: The talps or "layered pile" model. *Icarus* 187:332–344.

Beyer R. A. and McEwen A. S. 2005. Layering stratigraphy of eastern Coprates and northern Capri Chasmata, Mars. *Icarus* 179: 1–23.

Bibring J., Langevin Y., Mustard J. F., Poulet F., Arvidson R., Gendrin A., Gondet B., Mangold N., Pinet P., Forget F., and O. team 2006. Global mineralogical and aqueous Mars history derived from OMEGA/Mars Express data. *Science* 312:400–404.

Black B. A. and Stewart S. T. 2008. Impact crater geometries provide evidence for ice-rich layers at low latitudes on Mars. *Journal of Geophysical Research* 113(E02015), doi:10.1029/2007JE002888.

Boteler J. M. and Sutherland G. T. 2004. Tensile failure of water due to shock wave interactions. *Journal of Applied Physics* 96:6919–6924.

Bottke W. F., Nolan M. C., Greenberg R., and Kolvoord R. A. 1994. Collisional lifetimes and impact statistics of near-earth asteroids, in hazards due to comets and asteroids, edited by Gehrels T. Tucson: The University of Arizona Press. pp. 337–357.

Boyce J. M. and Garbeil H. 2007. Geometric relationships of pristine Martian complex impact craters, and their implications to Mars geologic history. *Geophysical Research Letters* 34, doi: 10.1029/2007GL029731.

Boyce J. M., Mouginis-Mark P., and Garbeil H. 2004. Predicted effects of surface processes on Martian impact crater depth/diameter relationships (abstract #2301). 35th Lunar and Planetary Science Conference. CD-ROM.

Boyce J. M., Mouginis-Mark P., and Garbeil H. 2005. Ancient oceans in the northern lowlands of Mars: Evidence from impact crater depth/diameter relationships. *Journal of Geophysical Research* 110(E3008), doi: 1029/2004JE002328.

Boyce J. M., Mouginis-Mark P., and Garbeil H. 2006. Deep impact craters in the Isidis and southwestern Utopia Planitia regions of Mars: High target material strength as a possible cause. *Geophysical Research Letters* 33, doi:10.1029/2005GL024462.

Boyce J. M. and Mouginis-Mark P. J. 2006. Martian craters viewed by the Thermal Emission Imaging System instrument: double-layered ejecta craters. *Journal of Geophysical Research* 111(E10), doi: 10.1029/2005JE002638.

Boynton W. V., Feldman W. C., Squyres S. W., Prettyman T. H., Bruckner J., Evans L. G., Reedy R. C., Starr R., Arnold J. R., Drake D. M., Englert P. A. J., Metzger A. E., Mitrofanov I.,Trombka J. I., d'Uston C., Wänke H., Gasnault O., Hamara D. K., Janes D. M., Marcialis R. L., Maurice S., Mikheeva I., Taylor G. J., Tokar R., and Shinohara C. 2002. Distribution of hydrogen in the near surface of Mars: Evidence for subsurface ice deposits. *Science* 297:81–85.

Bray V. J., Collins G. S., Morgan J. V., and Schenk P. M. 2008. The effect of target properties on crater morphology: Comparison of central peak craters on the Moon and Ganymede. *Meteoritics & Planetary Science* 43. This issue.

Byerlee J. 1978. Friction of rocks. *Pure and Applied Geophysics* 116: 615–626.

Cabrol N. A. and Grin E. A. 1999. Distribution, classification, and ages of Martian impact crater lakes. *Icarus* 142:160–172.

Carr M. H., Crumpler L. S., Cutts J. A., Greeley R., Guest J. E., and Masursky H. 1977. Martian impact craters and emplacement of ejecta by surface flow. *Journal of Geophysical Research* 82: 4055–4065.

Clifford S. M. 1993. A model for the hydrologic and climatic behavior of water on Mars. *Journal of Geophysical Research* 98(E6):10,973–11,016.

Clifford S. M. and D. Hillel 1983. The stability of ground ice in the equatorial region of Mars. *Journal of Geophysical Research* 88(NB3):2456–2474.

Cohn S. N. and Ahrens T. J. 1981. Dynamic tensile strength of lunar rock types. *Journal of Geophysical Research* 86(B3):1794–1802.

Collins G. 2002. Numerical modeling of large impact crater collapse, Ph.D. thesis, University of London. 235 p.

Collins G. S., Melosh H. J., and Ivanov B. A. 2004. Modeling damage and deformation in impact simulations. *Meteoritics & Planetary Science* 39:217–231.

Collins G. S. and Wünnemann K. 2005. How big was the Chesapeake Bay impact? Insight from numerical modeling. *Geology* 33:925–928.

Craddock R. A., Maxwell T. A., and Howard A. D. 1997. Crater morphometry and modification in the Sinus Sabaeus and Margaritifer Sinus regions of Mars. *Journal of Geophysical Research* 102(E6):13,321–13,340.

Crawford D. 1999. Adaptive mesh refinement in CTH. Paper presented at 15th U.S. Army Symposium on Solid Mechanics, U.S. Army, Myrtle Beach, SC, April 12–14.

Croft S. K., Kieffer S. W., and Ahrens T. J. 1979. Low-velocity impact craters in ice and ice-saturated sand with implications for Martian crater count ages. *Journal of Geophysical Research* 84(B14):8023–8032.

Durham W. B., Pathare A. V., and Stern L. A. 2008. The brittle-to-ductile transition of icy materials on Mars (abstract #2315). 39th Lunar and Planetary Science Conference. CD-ROM.

Edgett K. S. and Malin M. C. 2002. Martian sedimentary rock stratigraphy: Outcrops and interbedded craters of northwest Sinus Meridiani and southwest Arabia Terra. *Geophysical Research Letters* 29:2179–2182.

Fanale F. P., Postawko S. E., Pollack J. B., Carr M. H., and Pepin R. O. 1992. Mars: Epochal climate change and volatile history. In *Mars*, edited by Kieffer H. H., Jakosky B. M., Snyder C. W., Matthews M. S. Tucson: The University of Arizona Press. pp. 1135–1179.

Feistel R. and Wagner W. 2006. A new equation of state for H_2O ice Ih. *Journal of Physical and Chemical Reference Data* 35:1021–1047.

Feldman W. C., Boynton W. V., Tokar R. L., Prettyman T. H., Gasnault O., Squyres S. W., Elphic R. C., Lawrence D. J., Lawson S. L., Maurice S., McKinney G. W., Moore K. R., and Reedy R. C. 2002. Global distribution of neutrons from Mars: Results from Mars Odyssey. *Science* 297:75–78.

Forget F., Haberle R. M., Montmessin F., Levrard B., and Heads J. W. 2006. Formation of glaciers on Mars by atmospheric precipitation at high obliquity. *Science* 311:368–371.

Forsberg-Taylor N. K., Howard A. D., and Craddock R. A. 2004. Crater degradation in the Martian highlands: Morphometric analysis of the Sinus Sabaeus region and simulation modeling suggest fluvial processes. *Journal of Geophysical Research* 109(E05002), doi: 10.1029/2004JE002242.

Frank M. R., Fei Y., and Hu J. 2004. Constraining the equation of state of fluid H_2O to 80 GPa using the melting curve, bulk modulus, and thermal expansivity of Ice VII. *Geochimica et Cosmochimica Acta* 68:2781–2790.

Gault D. E. and Greeley R. 1978. Exploratory experiments of impact craters formed in viscous-liquid targets: Analogs for Martian rampart craters? *Icarus* 34:486–495.

Gault D. E., Quaide W. L., Oberbeck V. R., and Moore H. J. 1966. Luna 9 photographs: Evidence for a fragmental surface layer. *Science* 153:985–988.

Griffith A. A. 1920. The phenomena or rupture and flow in solids, *Philosophical Transactions of the Royal Society of London A* 34: 137–154.

Head J. N., Melosh H. J., and Ivanov B. A. 2002. Martian meteorite launch: High-speed ejecta from small craters. *Science* 298:1752–1756.

Head J. W., Marchant D. R., Agnew M. C., Fassett C. I., and Kreslavsky M. A. 2006. Extensive valley glacier deposits in the northern mid-latitudes of Mars: Evidence for Late Amazonian obliquity-driven climate change. *Earth and Planetary Science Letters* 241:663–671.

Head J. W., Mustard J. F., Kreslavsky M. A., Milliken R. E., and Marchant D. R. 2003. Recent ice ages on Mars. *Nature* 426:797–802.

Head J. W., Neukum G., Jaumann R., Hiesinger H., Hauber E., Carr M., Masson P., Foing B., Hoffmann H., Kreslavsky M.,Werner S., Milkovich S., and Gasselt van S. 2005. Tropical to mid-latitude snow and ice accumulation, flow and glaciation on Mars. *Nature* 434:346–351.

Herrmann W. 1969. Constitutive equation for the dynamic compaction of ductile porous materials. *Journal of Applied Physics* 40:2490–2499.

Hertel E. S., Jr. and Kerley G. 1998. *CTH reference manual: The equation of state package.* Report SAND98-0947, Sandia National Laboratories, Albuquerque, NM.

Hiraoka K., Arakawa M., and Nakamura A. M. 2006. Measurement of compressive and tensile strength of ice-silicate mixtures (abstract #1602). 37th Lunar and Planetary Science Conference. CD-ROM.

Holian K. S. 1984. T-4 *handbook of material properties data bases, vol. 1c: Equations of state.* Report LA-10160-MS, Los Alamos National Laboratory, Los Alamos, NM. 382 p.

Housen K. R. and Holsapple K. A. 1990. On the fragmentation of asteroids and planetary satellites. *Icarus* 84:226–253.

Housen K. R. and Holsapple K. A. 1999. Scale effects in strength-dominated collisions of rocky asteroids. *Icarus* 142:21–23.

Housen K. R. and Schmidt R. M. 1983. Crater ejecta scaling laws: Fundamental forms based on dimensional analysis. *Journal of Geophysical Research* 88(B3):2485–2499.

Jakosky B. M. and Carr M. H. 1985. Possible precipitation of ice at low latitudes of Mars during periods of high obliquity. *Nature* 559–561.

Kerley G. 1999. *Equations of state for composite materials.* Report KPS99-4. Albuquerque, NM: Kerley Publishing Services. 52 p.

Komatsu G., Ori G. G., Di Lorenzo S., Rossi A. P., and Neukum G. 2007. Combinations of processes responsible for Martian impact crater—"layered ejecta structures" emplacement. *Journal of Geophysical Research* 112(E6), doi:10.1029/2006JE002787.

Kormer S. B. 1968. Optical study of the characteristics of shock-compressed condensed dialectics. *Soviet Physics USPEKHI* 11: 229–254.

Krevslavsky M. A. and Head III J. W. 2006. Modification of impact craters in the northern plains of Mars: Implications for Amazonian climate history. *Meteoritics & Planetary Science* 41: 1633–1646.

Kring D. A. 2003. Potential habitats in impact-generated hydrothermal systems. *Geochimica et Cosmochimica Acta* 67: A236–A236.

Lange M. A. and Ahrens T. J. 1983. The dynamic tensile strength of ice and ice-silicate mixtures. *Journal of Geophysical Research* 88(B2):1197–1208.

Laskar J., Correia A. C. M., Gastineau M., Joutel F., Levrard B., and Robutel P. 2004. Long term evolution and chaotic diffusion of the insolation quantities of Mars. *Icarus* 170:343–364.

Levrard B., Forget F., Montmessin F., and Laskar J. 2004. Recent ice-rich deposits formed at high latitudes on Mars by sublimation of unstable equatorial ice during low obliquity. *Nature* 431:1072–1075.

Lindstrom M., Shuvalov V., and Ivanov B. 2005. Lockne crater as a result of marine-target oblique impact. *Planetary and Space Science* 53:803–815.

Lyzenga G. A., Ahrens T. J., Nellis W. J., and Mitchell A. C. 1982. The temperature of shock-compressed water. *Journal of Chemical Physics* 76:6282–6286.

Maeno N., Arakawa M., Yasutome A., Mizukami N., and Kanazawa S. 2003. Ice-ice friction measurements, and water lubrication and adhesion shear mechanisms. *Canadian Journal of Physics* 81:241–239.

Malin M. C. and Edgett K. S. 2000. Sedimentary rocks of early Mars. *Science* 290:1927–1937.

McGetchin T. R., Settle T. R., Head M., and Head J. W. 1973. Radial thickness variation in impact crater ejecta: Implications for lunar basin deposits. *Earth and Planetary Science Letters* 20:226–236.

McGlaun J. M., Thompson S. L., and Elrick M. G. 1990. CTH: A three-dimensional shock wave physics code. *Journal of Impact Engineering* 10:351–360.

Mellon M. T. and B. M. Jakosky 1995. The distribution and behavior of Martian ground ice during past and present epochs. *Journal of Geophysical Research* 100(E6):11781–11799.

Melosh H. J. and Ivanov B. A. 1999. Impact crater collapse. *Annual Reviews of Earth and Planetary Science* 27:385–415.

Meresse S. F., Costard F., Mangold N., Baratoux D., and Boyce J. M. 2006. Martian perched craters and large ejecta volume: Evidence for episodes of deflation in the northern lowlands. *Meteoritics & Planetary Science* 41:1647–1658.

Milliken R. E., Mustard J. F., and Goldsby D. L. 2003. Viscous flow features on the surface of Mars: Observations from high-resolution Mars Orbiter Camera (MOC) images. *Journal of Geophysical Research* 108(E6), doi:10.1029/2002JE002005.

Mischna M. A., Richardson M. I., Wilson R. J., and McCleese D. J. 2003. On the orbital forcing of Martian water and CO_2 cycles: A general circulation model study with simplified volatile schemes. *Journal of Geophysical Research* 108(E6), doi:10.1029/2003JE002051.

Mitrofanov I., Anfimov D., Kozyrev A., Litvak M., Sanin A.,Tret'yakov V., Krylov A., Shvetsov V., Boynton W., Shinohara C., Hamara D., and Saunders R. S. 2002. Maps of subsurface hydrogen from the high energy neutron detector, Mars Odyssey. *Science* 297:78–81.

Mouginis-Mark P. 1981. Ejecta emplacement and modes of formation of Martian fluidized ejecta craters. *Icarus* 45:60–76.

Mouginis-Mark P. J., Tornabene L. L., Boyce J. M., and McEwen A. S. 2007. Impact melt and water release at Tooting Crater, Mars (abstract #3039). Seventh International Conference on Mars. CD-ROM.

Mustard J. F., Cooper C. D., and Rifkin M. K. 2001. Evidence for recent climate change on Mars from the identification of youthful near-surface ground ice. *Nature* 412:411–414.

Neukum G., Jaumann J., Hoffmann H., Hauber E., Head J. W., Basilevsky A. T., Ivanov B. A., Werner S. C., Gasselt S. V., Murray J. B., McCord T., and HRSC 2004. Recent and episodic volcanic and glacial activity on Mars revealed by the High Resolution Stereo Camera. *Nature* 432:971–979.

Newsom H. E., Hagerty J. J., and Thorsos I. E. 2001. Location and sampling of aqueous and hydrothermal deposits in Martian impact craters. *Astrobiology* 1:71–87, doi:10.1089/153110701750137459.

Oberbeck V. R. 1975. The role of ballistic erosion and sedimentation in lunar stratigraphy. *Review of Geophysics and Space Physics* 13:337–362.

Oberbeck V. R. and Quaide W. L. 1967. Estimated thickness of a fragmental surface layer of Oceanus Procellarum. *Journal of Geophysical Research* 72:4697–4704.

Ormö J., Dohm J. M., Ferris J. C., Lepinette A., and Fairen A. G. 2004. Marine-target craters on Mars? An assessment study. *Meteoritics & Planetary Science* 39:333–346.

Ormö J., Shuvalov V. V., and Lindstrom M. 2002. Numerical modeling for target water depth estimation of marine-target impact craters. *Journal of Geophysical Research* 107(E12), doi: 10.1029/2002JE001865.

Owen T. 1992. The composition and early history of the atmosphere of Mars. In *Mars*, edited by Kieffer H. H., Jakosky B. M., Snyder C. W., Matthews M. S. Tucson: The University of Arizona Press. pp. 818–834.

Pathare A. V., Paige D. A., and Turtle E. 2005. Viscous relaxation of craters with the Martian south polar layered deposits. *Icarus* 174: 396–418.

Petrenko V. F. and Whitworth R. W. 1999. *Physics of ice.* New York: Oxford University Press. 392 p.

Phillips R. J., Zuber M. T., Solomon S. C., Golombek M. P., Jakosky B. M., Banerdt W. B., Smith D. E., Williams R. M. E., Hynekk B. M., Aharonson O., and S. A. H. II 2001. Ancient geodynamics and global-scale hydrology on Mars. *Science* 291:2587–2591.

Piekutowski A. J. 1977. Cratering mechanisms observed in laboratory-scale high-explosive experiments, in *Impact and explosion cratering*, edited by Roddy D. J., Pepin R. O., and Merrill R. B. New York: Pergamon Press. pp. 67–102.

Pierazzo E., Artemieva N. A., and Ivanov B. A. 2005. Starting conditions for hydrothermal systems underneath Martian craters: Hydrocode modeling. GSA Special Paper 384. Boulder: Geological Society of America. pp. 443–457.

Pike R. J. 1988. Geomorphology of impact craters on Mercury. In *Mercury*, edited by Chapman C. R., Matthews M. S., and Vilas F. Tucson: The University of Arizona Press. pp. 165–273.

Poulet F., Bibring J., Mustard J. F., Gendrin A., Mangold N., Langevin Y., Arvidson R. E., Gondet B., Gómez C., and team O. 2005. Phyllosilicates on Mars and implications for early Martian climate. *Science* 438:623–627.

Quaide W. L. and Oberbeck V. R. 1968. Thickness determinations of the lunar surface layer from lunar impact craters. *Journal of Geophysical Research* 73:5247–5270.

Rathbun J. A. and Squyres S. W. 2002. Hydrothermal systems associated with Martian impact craters. *Icarus* 157:362–372.

Sammonds P. R., Murrell S. A. F., and Rist M. A. 1998. Fracture of multiyear sea ice. *Journal of Geophysical Research* 103(C10) 21: 795–721,816.

Schenk P. M. 2002. Thickness constraints on the icy shells of the Galilean satellites from a comparison of crater shapes. *Nature* 417: 419–421.

Schultz P. H. 1992. Atmospheric effects on ejecta emplacement. *Journal of Geophysical Research* 97(E7):11,623–11,662.

Sekine T., Duffy T. S., Rubin A. M., Anderson W. W., and Ahrens T. J. 1995. Shock compression and isentropic release of granite. *Geophysical Journal International* 120:247–261.

Senft L. E. and Stewart S. T. 2007. Modeling impact cratering in layered surfaces. *Journal of Geophysical Research* 112(E11): doi:10.1029/2007JE002894.

Showman A. P. and Malhotra R. 1999. The Galilean satellites. *Science* 286:77–84.

Shuvalov V., Dypvik H., and Tsikalas F. 2002. Numerical simulations of the Mjølnir marine impact crater. *Journal of Geophysical Research* 107:5047.

Shuvalov V. V. and Trubestkaya I. A. 2002. Numerical modeling of marine target impacts. *Solar System Research* 36:417–430.

Stewart S. T. and Ahrens T. J. 2005. Shock properties of H_2O Ice. *Journal of Geophysical Research* 110(E03005), doi:10.1029/2004JE002305.

Stewart S. T., Seifter A., and Obst A. W. 2008. Measurements of emission temperatures from shocked H_2O ice (abstract #2301). 39th Lunar and Planetary Science Conference. CD-ROM.

Stewart S. T. and Valiant G. J. 2006. Martian subsurface properties and crater formation processes inferred from fresh impact crater geometries. *Meteoritics & Planetary Science* 41:1507–1537.

Swegle J. W. 1990. Irreversible phase transitions and wave propagation in silicate geologic materials. *Journal of Applied Physics* 68:1563–1579.

Tornabene L. L., McEwen A. S., Grant J. A., Mouginis-Mark P. J., Squyres S. W., Wray J. J., and HiRISE Science Team. 2007a. Evidence for the role of volatiles on Martian impact craters as revealed by HIRISE (abstract #2215). 38th Lunar and Planetary Science Conference. CD-ROM.

Tornabene L. L., McEwen A. S., Osinski G. R., Mouginis-Mark P. J., Boyce J. M., Williams R. M. E., Wray J. J., Grant J. A., and HiRISE Science Team. 2007b. Impact melting and the role of subsurface volatiles: Implications for the formation of valley networks and phyllosilicate-rich lithologies on early Mars (abstract #3288). Seventh International Conference on Mars. CD-ROM.

Wagner W. and Pruss A. 2002. The IAPWS formulation 1995 for the thermodynamic properties of ordinary water substance for general and scientific use. *Journal of Physical and Chemical Reference Data* 31:387–535.

Wünnemann K. and Ivanov B. A. 2003. Numerical modelling of the impact crater depth-diameter dependence in an acoustically fluidized target. *Planetary and Space Science* 51:831–845.

Zhang Y. 1999. A criterion for the fragmentation of bubbly magma based on brittle failure theory. *Nature* 402:648–650.

APPENDIX: A NEW TABULAR EOS FOR H_2O

The new EOS for H_2O includes ice Ih, ice VI, ice VII, liquid (L) and vapor (V). The table is gridded using 239 points in density (from 0 to 5000 kg/m^3) and 217 points in temperature (from 10 to 200,000 K). The spacing of the grid includes linear and logarithmic regions in order to resolve all phases and phase boundaries. A portion of the grid, with labeled phases, is shown in Fig. A1. In the construction of the table, at each grid point, the phase or phase boundary is identified and the internal energy, pressure and entropy are calculated.

The phase boundaries for the liquid and vapor phases (including boundaries to solid phases) are taken from the International Association for the Properties of Water and Steam (IAPWS) (Wagner and Pruss 2002). H_2O has 9 known stable solid phases and several metastable phases (Petrenko and Whitworth 1999); most of these phases occupy small regions of the phase diagram. The phase boundaries between the tabulated solid phases are therefore simplifications of the EOS. The included solid phases are those identified on the shock Hugoniot and known to be important for shock-induced melting (Stewart and Ahrens 2005).

The phase boundary between ice Ih and VI is artificial: the stable ice phases II, III, and V are neglected and the ice VI field is extended in pressure-temperature space to meet ice Ih near its equilibrium phase boundary given by Feistel and Wagner (2006). The tabulated Ih-VI boundary is linear with a slope of 0.2 MPa/K intersecting the experimental Ih-III-L triple point. The low-temperature ordered versions of ice Ih (ice XI) and ice VII (ice VIII) are neglected and these phases are extrapolated down to 10 K. The high-pressure, low temperature phase ice X is also neglected and ice VII is extrapolated to 5000 kg/m^3. The boundary between ice VI and liquid is the combination of the IAPWS melting curves for ices III, V, and VI. The tabulated boundary between ice VI and ice VII is linear with a slope of 1 MPa/K intersecting the experimental VI-VII-L triple point. The IAPWS melting curve for ice VII is extended to higher pressures using the experimental data from Frank et al. (2004).

The internal energy, pressure, and entropy for the liquid and vapor phases are calculated using the fortran code from the IAPWS. Values are extrapolated linearly to very high temperatures. The EOS for ice Ih is calculated using the equations given in Feistel and Wagner (2006). The internal energy and pressure for ice VI and VII are calculated using
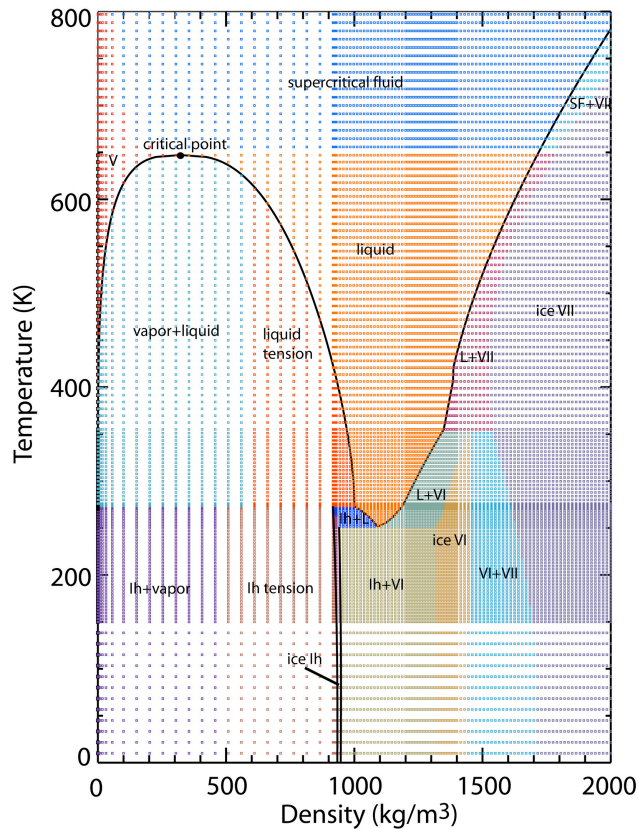
Fig. A1. Partial phase diagram of the tabular H$_2$O equation of state, showing phases and phase boundaries.

Fig. A2. Calculated shock Hugoniots for 200 K ice (solid line) and 300 K liquid water (dashed line).

the equations given in Stewart and Ahrens (2005). In ice VI and VII, isentropes are assumed to be approximately equal to isotherms and intersect the entropies provided by the IAPWS at the melting curves. Note that CTH uses the internal energy and pressure but not the entropy in the table. Entropy is included for ease of calculation of isentropes. The internal energy and entropies along phase boundaries are calculated by weighting the end member values by mass fraction.

The table includes tension regions for ice Ih (to −2 GPa) and liquid (to −0.3 GPa). The tension region occupies a portion of the equilibrium mixed regions between ice Ih-vapor and liquid-vapor. The volume expansion under tension is approximated by a 3rd order Birch-Murnaghan equation, and the internal energy and entropies are extrapolated from the low-pressure region into the tension region.

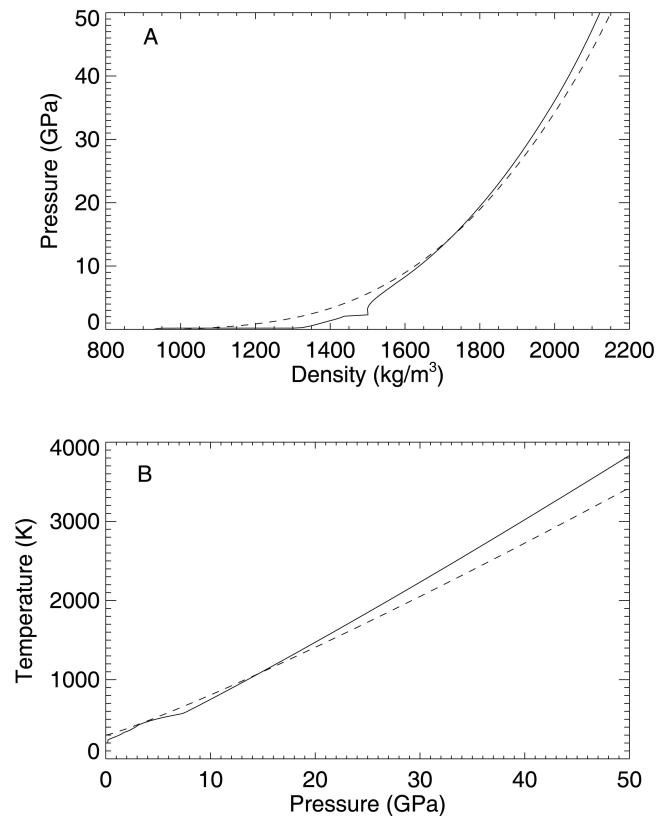Ice and liquid water shock Hugoniots, derived from the

tabular EOS, are shown in Fig. A2 in pressure-density and pressure-temperature space. Note that the crossing of the ice and liquid water Hugoniots is expected because the less dense ice is more compressible and has a larger thermal component at high shock pressures compared to liquid water (Stewart and Ahrens 2005). The critical shock pressures for melting are in good agreement with Stewart and Ahrens (2005). The critical shock pressures for vaporization are in good agreement with estimates from Stewart and Ahrens (2005) and experimental measurements of post-shock temperatures (Stewart et al. in preparation). Under Martian conditions (~200 K, 600 Pa), the critical shock pressures are 1 and 2.9 GPa for incipient and complete melting, and 2.9 and 63 GPa for incipient and complete vaporization. Note that the criteria for complete melting and incipient vaporization are the same because the reference pressure is the triple point for H$_2$O. Future work will refer to this table as the "5-Phase" EOS.